Chapter 10

Envelope estimation for quasi-periodic geophysical signals in noise: a multitaper approach

J. Park

10.1 Introduction

Many processes in nature are quasi-periodic, and can be represented as having a dominant oscillation with carrier frequency f_0 that suffers amplitude and phase variations on a time scale T_1 much longer than the oscillation period $T_0 = 1/f_0$. Quasi-periodicity is characteristic of certain deterministic classical mechanical systems, such as fluctuations in the Earth's orbital parameters, and resonant systems subject to stochastic excitation, such as the atmospheric southern oscillation. Systems with many periodic oscillations that are closely spaced in frequency, such as the Earth's free oscillation spectrum, are often observed as quasi-periodic. Data collected from these processes take the form $u_n = \Re\{A_n e^{-2\pi i f_0 n\Delta t}\}$, $n = 1, 2, \ldots, N$ for duration $T = N\Delta t$. The slowly varying complex-valued envelope* $A_n = A(n\,\Delta t)$ can be represented as a narrow-band function $\bar{A}(f)$ in the frequency domain: in particular,

$$A(n\,\Delta t) = A_n = \int_{-f_N}^{f_N} \bar{A}(f) e^{-2\pi i f n\Delta t}\, df, \tag{10.1}$$

where $f_N = 1/(2\,\Delta t)$ is the Nyquist frequency. We assume that $\bar{A}(f) \approx 0$ for $|f| > f_w$ for some half-bandwidth f_w, so that it has minimum time scale of variation $T_1 = 1/f_w$. In some situations, however, the envelope of a quasi-periodic signal may undergo sudden changes, e.g. the impulsive excitation of an oscillatory system, or a bifurcation in a chaotic system. Such behavior 'broadens' $\bar{A}(f)$. In most practical situations, however, the quasi-periodic signal is one component of a 'mixed' spectrum containing additional broad-band stochastic processes, e.g. noise. Often $|\bar{A}(f)|$ is comparable to the

* The 'amplitude' of the envelope – the quantity that is most easy to visualize – is the modulus of the complex-valued envelope.

broadband spectrum outside some narrow bandwidth $[-f_w, f_w]$, and one is faced with reconstructing the envelope A_n, $n = 1, 2, \ldots, N$, from spectral information inside $[-f_w, f_w]$ only.

Narrow-band filtering is a common method for analysing quasi-periodic signals. In this chapter a new technique based on multiple-taper spectrum analysis (Thomson, 1982; Park *et al.*, 1987b; Walden, 1990) is presented. The multitaper approach allows the analyst to model the envelope function $A(t)$ using the tools of inverse theory. This approach allows one to solve for the envelope function that fits the time-series data while optimizing some property of the envelope. The use of the term 'inverse theory' in this context can be misleading. Geophysicists differ over what comprises inverse theory, especially over how to deal with the fact that, in most examples, infinitely many models can fit a given finite data set. The approach of Tarantola (1987) seeks the model that is most consistent with *a priori* statistical information about model parameters. Others take a 'strict bounds' approach (e.g. Stark *et al.*, 1986), in which one seeks characteristics common to all models that satisfy a finite data set and a set of *a priori* constraints. The approach of this report is less sophisticated than either of the above examples, but closer in spirit to the former. Discrimination between different models often involves criteria specific to the application, so that the proper choice of *a priori* constraints is part of the research problem to be solved. We develop a flexible set of tools to test hypotheses about quasi-periodic signals in time series, in particular, to investigate the effect of possible discontinuous changes in amplitude and phase.

We use the techniques of multiple-taper spectrum analysis, as these offer spectrum estimators that are optimally band-limited. In the next section we derive inversion algorithms that find the 'smallest' and 'smoothest' envelopes that fit data from a given time series, and show results from synthetic test examples. We generalize the algorithms to model sudden changes in the envelope, and compensate for background 'noise' and data gaps. We show analyses of time series from both long-period seismograms and analysis of sediment cores. Section 10.3 examines seismic data from the great Macquarie Ridge earthquake of 23 May 1989. Section 10.4 examines quasi-periodic changes in Earth climate from the last 2.7 My as recorded by oxygen isotope fluctuations in an oceanic sediment core.

10.2 The inverse problem for an oscillation envelope

If $\bar{A}(f) \approx 0$ for $|f| > f_w$, it is natural to seek an expansion for $\bar{A}(f)$ in terms of a basis set of functions $W(f)$ over $[-f_w, f_w]$. A basis set of the discrete prolate spheroidal wavefunctions $W_k(f)$ (Thomson, 1982; Slepian, 1983) possesses the useful feature that the $W_k(f)$ are orthogonal both on the frequency interval $[-f_w, f_w]$ and the interval $[-f_N, f_N]$. The $W_k(f)$ are the discrete

Fourier transform pairs of time-domain data 'eigentapers' $w_n^{(k)}$, $n = 1, \ldots, N$:

$$W_k(f) = \sum_{n=1}^{N} w_n^{(k)} e^{2\pi i f n \Delta t}$$

$$w_n^{(k)} = \int_{-f_N}^{f_N} W_k(f) e^{2\pi i f n \Delta t} \, df = \lambda_k^{-1} \int_{-f_w}^{f_w} W_k(f) e^{2\pi i f n \Delta t} \, df \qquad (10.2)$$

and satisfy the condition that the functional

$$\lambda(W) = \frac{\int_{-f_w}^{f_w} |W(f)|^2 \, df}{\int_{-f_N}^{f_N} |W(f)|^2 \, df} \qquad (10.3)$$

is stationary. Larger values of the functional occur for functions that are concentrated in the narrow band $[-f_w, f_w]$. Note that $\lambda < 1$ if $f_w < f_N$, because any taper is time-limited, and therefore cannot have a totally band-limited spectrum (Slepian, 1983). The eigentapers satisfy an $N \times N$ matrix eigenvalue problem

$$\mathscr{A} \cdot \mathbf{w}_k = \lambda_k \mathbf{w}_k, \qquad (10.4)$$

where $\mathscr{A}_{nm} = 2 \Delta t f_w \operatorname{sinc}(2\pi f_w (n-m) \Delta t)$ and $\mathbf{w}_k$ is an N-vector containing the kth eigentaper. From eq. (10.4) there are N orthogonal eigentapers for a time series with N data, with eigenvalues λ_k, equivalent to the stationary values of (10.3). We take the normalization convention $\mathbf{w}_k \cdot \mathbf{w}_l = \delta_{kl}$, so that $\mathbf{w}_k \cdot \mathscr{A} \cdot \mathbf{w}_k = \int_{-f_w}^{f_w} |W_k(f)|^2 \, df = \lambda_k$, and order $1 > \lambda_0 > \lambda_1 > \lambda_2 > \cdots > \lambda_{N-1} \geqslant 0$. The eigenvalues λ_k measure the spectral leakage resistance of the eigentapers $w_n^{(k)}$. Eigentapers with $\lambda \approx 1$ can be used to construct spectrum estimates that are resistant to spectral leakage. If $f_w = pf_R$, where $f_R = 1/T = 1/(N \Delta t)$ is the Rayleigh frequency of the time series, the first $2p - 1$ eigentapers have sufficient spectral leakage resistance to be useful in spectrum analysis. Tapers constructed for $f_w = pf_R$ (p need not be an integer) are called $p\pi$-prolate Slepian tapers (Figure 10.1), following the terminology of Thomson (1990). Methods for using Slepian tapers to construct general-purpose spectrum estimators are described by Thomson (1982), Park *et al.* (1987b), Walden (1990) and Thomson (1990).

If $A(f) = 0$ outside the narrow band $[-f_w, f_w]$, the behavior of $\bar{A}(f)$ that is resolvable with the N-point data series is an expansion of the prolate spheroidal wavefunctions:

$$\bar{A}(f) = \sum_{k=0}^{N-1} a_k W_k(f) \qquad (10.5)$$

for $f \leqslant f_w$, so that

$$A(n \Delta t) = A_n = \sum_{k=0}^{N-1} \int_{-f_w}^{f_w} a_k W_k(f) e^{-2\pi i f n \Delta t} = \sum_{k=0}^{N-1} \lambda_k a_k w_n^{(k)}. \qquad (10.6)$$

The coefficient a_k is related directly to the discrete Fourier transform (DFT)

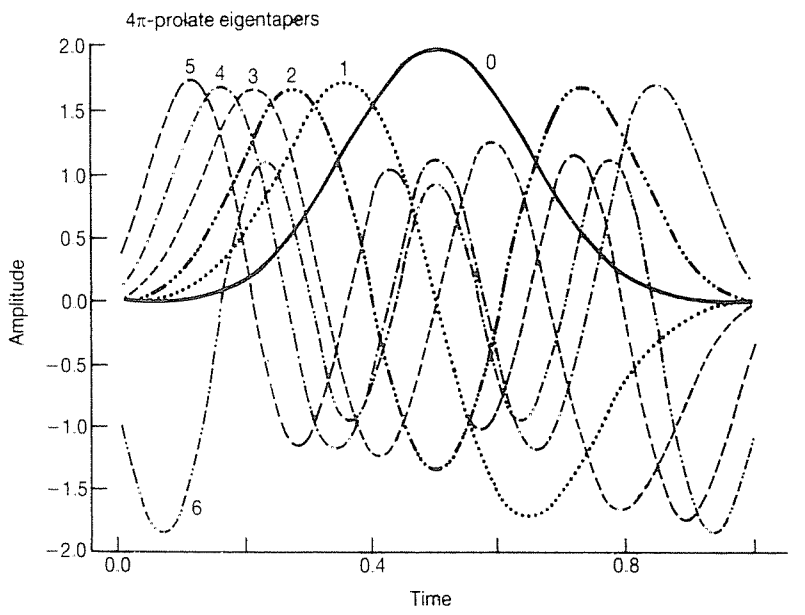

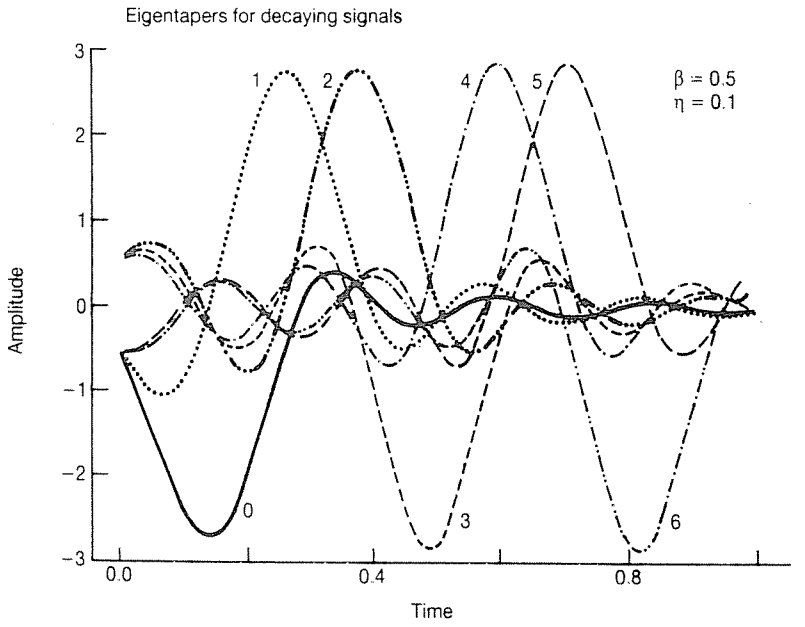

Figure 10.1 (a) The first seven 4π-prolate Slepian tapers. The tapers are constructed with time–bandwidth product $p = 4$, which corresponds to a half-width of $f_w = 4f_R = 4/T$ for the associated convolution kernels in the frequency domain. (b) The first seven Slepian tapers with time–bandwidth product $p = 4$, designed for signals that decay by $\beta = 0{\cdot}5Q$ cycles (a factor of $e^{-\pi}$) within a data series, and white-noise weighting parameter $\eta = 0{\cdot}1$.

of the data series $u_1, u_2, \ldots, u_N$ tapered by the kth Slepian taper $w_n^{(k)}$. The complex-valued DFT evaluated at f_0 is the kth eigenspectrum estimate $Y_k(f_0)$, where

$$Y_k(f_0) = \sum_{n=1}^{N} w_n^{(k)} u_n e^{2\pi i f_0 n \Delta t} = \sum_{n=1}^{N} w_n^{(k)} A_n = \lambda_k a_k. \tag{10.7}$$

If $\bar{A}(f) \neq 0$ outside $[-f_w, f_w]$, spectral leakage will bias values of a_k, especially for eigenspectra calculated with higher-order Slepian tapers with λ_k significantly less than unity. In practical situations one must truncate (10.5) at some $K \leqslant 2p-1$ to minimize spectral leakage bias. For some chosen truncation K, we can estimate the envelope A_n with B_n, $n = 1, \ldots, N$, where

$$B_n = \sum_{k=0}^{K-1} \lambda_k^{-1} Y_k(f_0) w_n^{(k)}. \tag{10.8}$$

This is the multi-taper complex demodulate at the carrier frequency f_0 (Thomson, 1990). In this formula, the tapers $w_n^{(k)}$ are real-valued, while the eigenspectra $Y_k(f_0)$ and therefore the complex demodulate B_n are complex-valued. The proper choice of K will depend on the particular data series, as the analyst seeks to balance resistance to spectral leakage against obtaining a maximum number of data constraints. Thomson (1982) uses 4π-prolate Slepian tapers and chooses $K = 5 < 2p - 1 = 7$ eigentapers for multi-taper estimation of highly colored spectra. In most situations involving envelope estimation, however, a quasi-periodic signal in a data series attracts scrutiny because the signal appears as a prominent peak in the estimated Fourier spectrum. In this case, spectral leakage is less problematic and $K = 2p - 1$ is an appropriate choice. It is possible to downweight the influence of the higher-order eigenspectra without discarding them; this is discussed near the end of this section (eq. (10.21)).

Equation (10.8) is a valid model for the oscillation envelope A_n, but it is not the only valid model. For instance, a constant envelope $A_n \equiv A_0$ cannot be represented by any weighted sum of the first few Slepian tapers, but is often a most reasonable physical model. More flexibility is gained by treating the estimation of A_n as a standard linear inverse problem (Parker, 1977; Menke, 1984). Let $\mathbf{B} = (B_1, B_2, \ldots, B_N)$ be the 'model' for the oscillation envelope $\mathbf{A} = (A_1, A_2, \ldots, A_N)$. We have K 'data constraints'

$$Y_k(f_0) = \sum_{n=1}^{N} w_n^{(k)} A_n = \mathbf{g}_k \cdot \mathbf{A}, \tag{10.9}$$

which identify K data kernels $\mathbf{g}_k = \mathbf{w}_k$. It is a standard consequence of the projection theorem in inner-product spaces that the model $\mathbf{B}$ that fits the K data constraints while minimizing $\|\mathbf{B}\|^2 = \mathbf{B} \cdot \mathbf{B}$ is a linear combination of the data kernels $\mathbf{g}_k$. This minimum-size solution for the envelope is given by (10.8), a linear combination of the Slepian tapers. Define a data vector $\mathbf{y} = (Y_0(f_0), \ldots, Y_{K-1}(f_0))$, a coefficient vector $\mathbf{a} = (a_0, \ldots, a_{K-1})$ and a $K \times N$ kernel matrix $\mathbf{G}$ whose rows are the data kernels $\mathbf{g}_k$. If we form a Gram matrix $\mathbf{\Gamma} = \mathbf{G} \cdot \mathbf{G}^{\mathrm{T}}$, where $\Gamma_{kl} = \mathbf{g}_k \cdot \mathbf{g}_l$, the formal solution for this expansion is $\mathbf{a} = \mathbf{\Gamma}^{-1} \cdot \mathbf{y}$. In the minimum-size solution (10.8), the orthogonality of the $\mathbf{g}_k$ renders the Gram matrix $\mathbf{\Gamma}$ diagonal.

Once the linear inverse problem is formulated, other solutions $\mathbf{B}$ can be found that minimize other quadratic functionals. In addition, one can solve for an envelope that deviates least from some preferred model $\mathbf{w}^{(0)}$, e.g. a constant envelope, or an exponentially decaying envelope. We can construct an envelope solution of the form

$$\mathbf{B} = b\mathbf{w}^{(0)} + \sum_{k=0}^{K-1} a_k \mathbf{g}_k = b\mathbf{w}^{(0)} + \mathbf{G}^{\mathrm{T}} \cdot \mathbf{a}, \tag{10.10}$$

where b and the K-vector $\mathbf{a}$, both complex-valued, are to be determined. A solution of this form obtains oscillation envelopes that are closest to a scalar multiple of $\mathbf{w}^{(0)}$ in the sense of minimizing $\|\mathbf{B} - b\mathbf{w}^{(0)}\|^2$. To obtain a unique solution we specify that the terms on the right sides of (10.10) are mutually orthogonal, leading to the equations

$$\begin{aligned} b\mathbf{z} + \boldsymbol{\Gamma} \cdot \mathbf{a} &= \mathbf{y} \\ \mathbf{z} \cdot \mathbf{a} &= 0, \end{aligned} \tag{10.11}$$

where $z_k = \mathbf{g}_k \cdot \mathbf{w}^{(0)}$. Multiply the first equation by $\mathbf{z} \cdot \boldsymbol{\Gamma}^{-1}$ to obtain the formal solution

$$\begin{aligned} b &= (\mathbf{z} \cdot \boldsymbol{\Gamma}^{-1} \cdot \mathbf{y})/(\mathbf{z} \cdot \boldsymbol{\Gamma}^{-1} \cdot \mathbf{z}) \\ \mathbf{a} &= \boldsymbol{\Gamma}^{-1} \cdot (\mathbf{y} - b\mathbf{z}). \end{aligned} \tag{10.12}$$

Numerical efficiency can be gained by avoiding the calculation of $\boldsymbol{\Gamma}$ and its inverse by using the QR decomposition (Lawson and Hanson, 1974) of the kernel matrix $\mathbf{G}$. Let $\mathbf{G}^{\mathrm{T}} = \mathbf{Q} \cdot \mathbf{R}$, where $\mathbf{Q}$ is an $N \times K$ matrix with orthonormal columns and $\mathbf{R}$ is a $K \times K$ upper triangular matrix. The $K \times K$ identity matrix $\mathbf{I} = \mathbf{Q}^{\mathrm{T}} \cdot \mathbf{Q}$, and the $N \times N$ matrix $\mathbf{Q} \cdot \mathbf{Q}^{\mathrm{T}}$ is an orthogonal projection matrix from R^N onto the subspace spanned by the kernel vectors $\mathbf{g}_k$. After some manipulation, the solution for an oscillation envelope of the form (10.10) is

$$\mathbf{B} = b\mathbf{w}^{(0)} + \mathbf{Q} \cdot ((\mathbf{R}^{\mathrm{T}})^{-1} \cdot \mathbf{y} - b\mathbf{Q}^{\mathrm{T}} \cdot \mathbf{w}^{(0)}), \tag{10.13}$$

where $b = (\mathbf{w}^{(0)} \cdot \mathbf{Q} \cdot (\mathbf{R}^{\mathrm{T}})^{-1} \cdot \mathbf{y})/(\mathbf{w}^{(0)} \cdot \mathbf{w}^{(0)})$. Since $\mathbf{R}$ is upper triangular, $(\mathbf{R}^{\mathrm{T}})^{-1} \cdot \mathbf{y}$ can be calculated efficiently by back-substitution.

To obtain smooth envelopes consistent with measured eigenspectra we use a variation of Occam's inversion (Constable *et al.*, 1987) suggested by Parker (1990). Consider the approximate first-difference operator $\mathbf{D} = D_{ij}$, an $N \times N$ matrix with $D_{11} = \varepsilon \ll 1$, $D_{ii} = 1$ for $i > 1$, $D_{i-1,i} = -1$ and $D_{ij} = 0$ otherwise. The inverse of this matrix is a crude integration operator $\mathbf{D}^{-1}$, where $D_{1i}^{-1} = \varepsilon^{-1}$, $D_{ij}^{-1} = 1$ for $1 < i \leqslant j$, and $D_{ij}^{-1} = 0$ for $j < i$. The data constraints (10.9) can be rewritten as

$$Y_k(f_0) = \mathbf{w}_k \cdot \mathbf{D}^{-2} \cdot \mathbf{D}^2 \cdot \mathbf{A} = \tilde{\mathbf{g}}_k \cdot \tilde{\mathbf{A}}, \tag{10.14}$$

where $\tilde{\mathbf{g}}_k = \mathbf{w}_k \cdot \mathbf{D}^{-2}$ and $\tilde{\mathbf{A}} = \mathbf{D}^2 \cdot \mathbf{A}$. An envelope $\mathbf{B}$ that satisfies the 'data constraints' while minimizing

$$\|\mathbf{D}^2 \cdot \mathbf{B}\|^2 = \sum_{n=2}^{N-1} (B_{n+1} - 2B_n + B_{n-1})^2 + (B_2 - (1+\varepsilon)B_1)^2 + \varepsilon^4 B_1^2 \tag{10.15}$$

can be constructed from $\mathbf{D}^{-2} \cdot \tilde{\mathbf{B}}$, where $\tilde{\mathbf{B}}$ is a linear combination of the $\tilde{\mathbf{g}}_k$. The first term on the right-hand side of (10.15) measures the roughness of the envelope. The extra terms in (10.15) complicate the interpretation of $\mathbf{B} = \mathbf{D}^{-2} \cdot \sum_{k=0}^{K-1} \tilde{a}_k \tilde{\mathbf{g}}_k$ as the 'smoothest' model for the oscillation envelope $\mathbf{A}$. The extra terms constrain envelope models for which $\sum_{n=2}^{N-1} (B_{n+1} - 2B_n + B_{n-1})^2 = 0$, e.g. constant vectors and linear ramps. In numerical tests (performed with 8-byte floating-point-precision VAX/VMS Fortran) their influence on the solution roughness appears negligible for $N > 100$ data points and $\varepsilon \leqslant 10^{-4}$. However, the sensitivity to ε may depend somewhat on the computer precision and on the values of N, K and p.

An alternative approach is seminorm minimization (Parker *et al.*, 1987), which can solve for constant and linear-ramp envelopes explicitly, while applying a roughness penalty on the remainder of the solution. We adopt one aspect of the seminorm approach and solve for a 'fixed element' $\mathbf{w}^{(0)}$ as well as a solution that minimizes (10.15). We can construct an estimate for $\tilde{\mathbf{A}}$ of the form

$$\tilde{\mathbf{B}} = \tilde{b}\tilde{\mathbf{w}}^{(0)} + \sum_{k=0}^{K-1} \tilde{a}_k \tilde{\mathbf{g}}_k = \tilde{b}\tilde{\mathbf{w}}^{(0)} + \tilde{\mathbf{G}}^{\mathrm{T}} \cdot \tilde{\mathbf{a}}, \tag{10.16}$$

where $\tilde{\mathbf{w}}^{(0)} = \mathbf{D}^2 \cdot \mathbf{w}^{(0)}$, $\tilde{\mathbf{G}}$ is a $K \times N$ matrix whose kth row is $\tilde{\mathbf{g}}_{k-1}$ and $\tilde{b}$, $\tilde{\mathbf{a}}$ are to be determined. The oscillation envelope $\mathbf{B} = \mathbf{D}^{-2} \cdot \tilde{\mathbf{B}}$ is the solution closest to a scalar multiple of $\mathbf{w}^{(0)}$ in the sense of minimizing $\|\mathbf{D}^2 \cdot (\mathbf{B} - \tilde{b}\mathbf{w}^{(0)})\|^2$. The 'smooth' data kernels $\tilde{\mathbf{g}}_k$ are not orthogonal, and the associated Gram matrix $\tilde{\boldsymbol{\Gamma}}$ is full, though symmetric. Since the 'data' constraints can be written as $\tilde{\mathbf{G}} \cdot \tilde{\mathbf{B}} = \mathbf{y}$, formulae for $\tilde{b}$, $\tilde{\mathbf{a}}$ and $\tilde{B}$ are straightforward generalizations of (10.11)–(10.13).

Four generalizations of the above development are useful:

(1) In many physical processes an oscillation suffers a sudden shift in amplitude and phase, but is otherwise slowly varying. In long-period seismology, this would occur if a second seismic event (e.g. an aftershock) re-excited the free oscillations. The first-difference matrix $\mathbf{D}$ can be partitioned at a chosen breakpoint $\tilde{N} < N$:

$$\tilde{\mathbf{D}} = \begin{bmatrix} \mathbf{D}^{(\tilde{N})} & \mathbf{0} \\ \mathbf{0} & \mathbf{D}^{(N-\tilde{N})} \end{bmatrix}, \tag{10.17}$$

where $\mathbf{D}^{(M)}$ is an $M \times M$ first-difference matrix. This partitioned matrix and its inverse can be used to set up the linear inverse problems, similar to (10.11), for envelopes that can have discontinuities at the chosen breakpoint, but are constrained to be smooth elsewhere.

(2) Seismic data records often have segments of bad or missing data due to instrument failure or nonlinearity. Therefore edited data records used for analysis often have gaps. The effect of gaps on data spectrum estimates can be modeled by introducing identical gaps in the data tapers $\mathbf{w}_k$. An envelope estimate derived from (10.16) will interpolate the gap with a sum of a third-order polynomial and the fixed element $\mathbf{w}^{(0)}$.

(3) The third generalization applies when the desired carrier frequency f_0

does not equal one of the discrete frequencies of the numerical fast Fourier transform. If we choose eigenspectra $Y(\hat{f}_0)$ at a nearby FFT frequency $\hat{f}_0$ for analysis, the K real-valued data kernels $\mathbf{g}_k$ in (10.9) become complex-valued vectors and eq. (10.7) becomes

$$Y_k(\hat{f}_0) = \sum_{n=1}^{N} w_n^{(k)} u_n e^{2\pi i \hat{f}_0 n \Delta t} = \sum_{n=1}^{N} w_n^{(k)} A_n e^{2\pi i (\hat{f}_0 - f_0) n \Delta t} = \mathbf{g}_k \cdot \mathbf{A}, \tag{10.18}$$

where $(\mathbf{g}_k)_n = w_n^{(k)} e^{2\pi i (\hat{f}_0 - f_0) n \Delta t}$. The Gram matrix $\mathbf{\Gamma}$ becomes complex-Hermitian rather than real-symmetric, with $\Gamma_{kl} = \mathbf{g}_k \cdot \mathbf{g}_l^*$ (the asterisk denotes complex conjugation), and the QR decomposition involves complex-valued matrices. Otherwise the solution algorithm is similar.

(4) Park *et al.* (1987a) and Lindberg and Park (1987) extended the definition of the bandwidth concentration functional (10.4) to design Slepian tapers for decaying signals in the presence of stationary noise. These tapers satisfy the generalized eigenvalue problem

$$\tilde{\mathscr{A}} \cdot \mathbf{w}_k = \tilde{\lambda}_k \tilde{\mathscr{C}} \cdot \mathbf{w}_k, \tag{10.19}$$

where $\tilde{\mathscr{A}}_{nm} = 2\,\Delta t\, f_w\, \mathrm{sinc}\,(2\pi f_w (n-m)\,\Delta t) e^{-\alpha(n+m)\Delta t}$ and $\tilde{\mathscr{C}}_{nm} = (e^{-\alpha(n+m)\Delta t} + \eta)\delta_{nm}$. The factor α is the decay rate of the oscillation and η is a weighting parameter that scales the sensitivity of the tapers to stationary noise. The amplitude of an oscillation with quality factor Q will decay by a factor of $e^{-\beta\pi}$ after βQ cycles. Tapers are constructed for chosen parameters η and a total decay of βQ oscillation cycles. If background noise is ignored, $\eta = 0$, and the optimal tapers will be the stationary-signal data tapers (Figure 10.1(a)) multiplied by an increasing exponential. Examples of 4π-prolate tapers designed for $\beta = 0{\cdot}5$ and $\eta = 0{\cdot}1$ are shown in Figure 10.1(b). Additional help in modeling envelopes that suffer exponential decay can be obtained by removing βQ-cycles of exponential growth from the specialized tapers before constructing the data kernels $\mathbf{g}_k$. Formally, this involves a renormalization of the data constraints similar to (10.14). Define an $N \times N$ matrix $\mathbf{E} = \mathrm{diag}\{e^{\beta\pi/N}, e^{2\beta\pi/N}, \ldots, e^{\beta\pi}\}$ and rewrite the data constraints $Y_k(f_0) = \mathbf{w}_k \cdot \mathbf{E}^{-1} \cdot \mathbf{E} \cdot \mathbf{A} = \tilde{\mathbf{g}}_k \cdot \tilde{\mathbf{A}}$ and modify the roughness penalty function (10.15) accordingly. If one solves for $\mathbf{E} \cdot \mathbf{B}$ rather than $\mathbf{B}$ (in practice this is achieved by skipping the last renormalization of the inverse solution $\tilde{\mathbf{B}}$ from (10.16)), we obtain a model for the envelope of the quasi-periodic signal with the decay removed.

We show two synthetic examples to contrast different approaches for estimating an oscillation envelope $A(t)$. We compare solutions of the form (10.10) and (10.16), that is, size versus roughness constraints. Figure 10.2 shows two test oscillations with $f_0 = \frac{1}{6}$ mHz. For test series A both the amplitude and phase of $A(t)$ vary as a second-degree polynomial in t. The second test series (B) suffers an abrupt change in amplitude and phase at its midpoint, but varies smoothly elsewhere. We construct solutions using seven 4π-prolate Slepian tapers $\mathbf{w}_k$ and a constant amplitude fixed element $\mathbf{w}^{(0)}$. Figure 10.3 graphs the modeled amplitude and phase of $A(t)$ against the

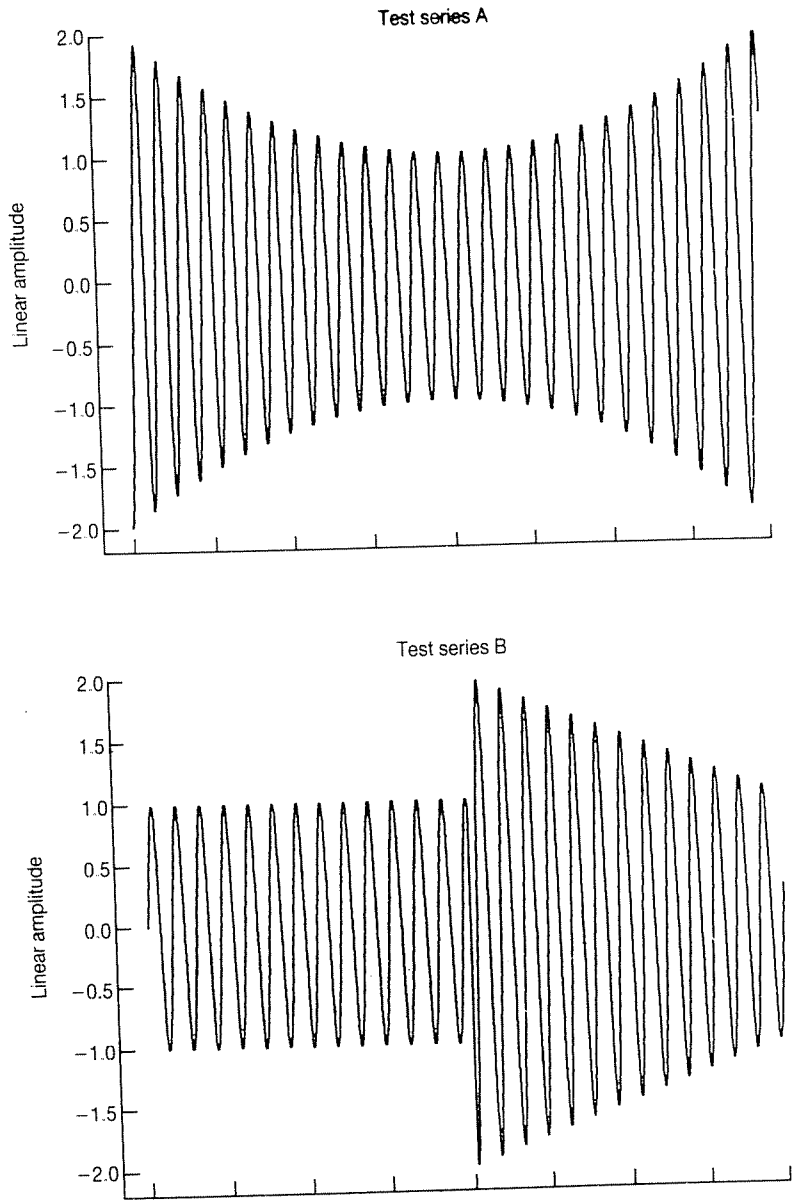

Figure 10.2 Synthetic test series for envelope estimation.

theoretical values for the first synthetic. The smooth model $\mathbf{D}^{-2} \cdot \tilde{\mathbf{B}}$ for the envelope is more successful at following the smooth variation in $A(t)$. Figure 10.4 graphs three models for the envelope of the second synthetic. In addition to the two solutions (10.10) and (10.16), a third model partitions $\mathbf{D}$ at the midpoint of the time series, allowing a discontinuity. All models detect

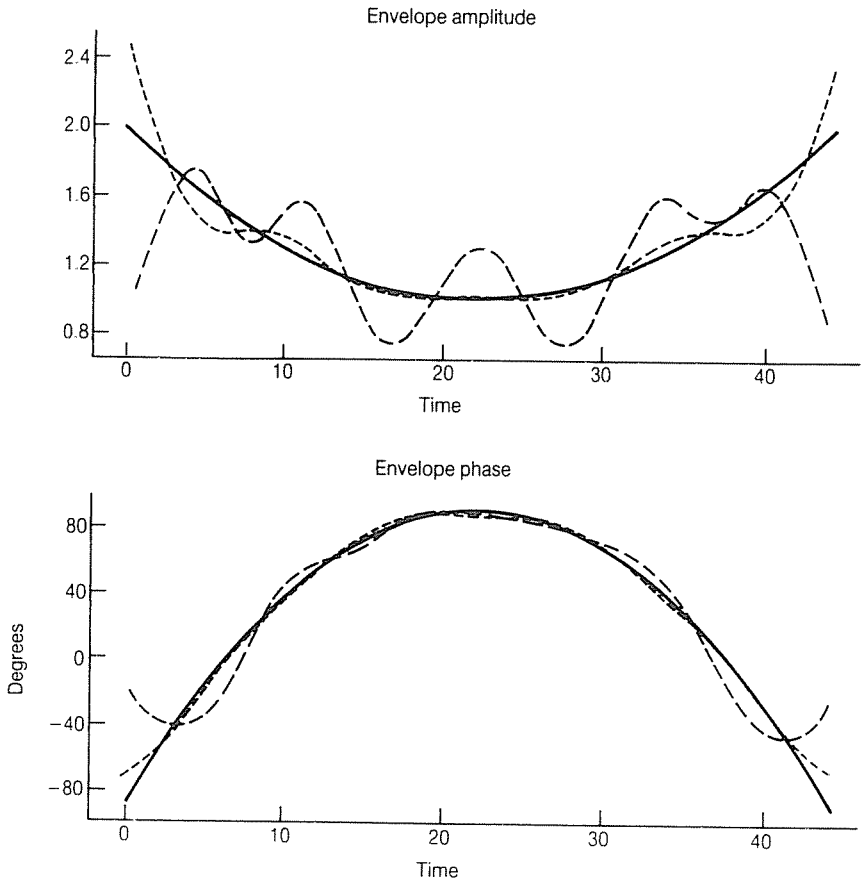

Figure 10.3 Envelope estimators for test series A, using eigenspectra computed with the seven 4π-prolate tapers shown in Figure 10.1. The solid line is the exact amplitude and phase. The coarse-dashed line is a solution of form (10.10), the envelope that is the smallest deviation from constant amplitude and phase. The fine-dashed line is a solution of form (10.16), the envelope that is the smoothest deviation from constant amplitude and phase.

a rapid change in phase, but only the inversion that allows a breakpoint follows well the abrupt change in $|A(t)|$. An incorrect choice of breakpoint leads to much more complicated models (Figure 10.5).

All of the above solutions fit the 'data' (the eigenspectra $Y_k(f_0)$) within numerical precision. Infinitely many envelopes will fit the 'data' equally well, because the inverse problem for $A(t)$ is non-unique. A large proportion of this infinity of models, however, corresponds to $\bar{A}(f)$ with large amplitude outside $[-f_w, f_w]$. In practical situations it is prudent to use for interpretation the smoothest model that fits the data, for it suppresses features that are not required by the data, and leads to models that are reasonably band-limited.

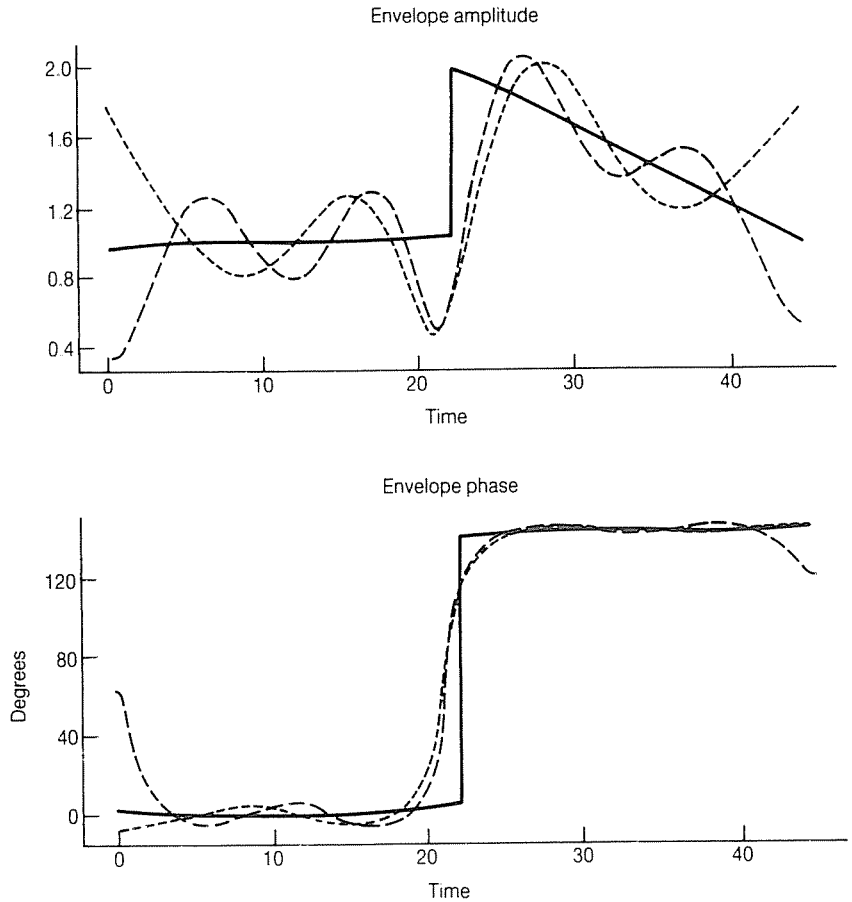

Figure 10.4 Envelope estimators for test series B, using eigenspectra computed with the seven 4π-prolate tapers shown in Figure 10.1. The coarse-dashed line is a solution of form (10.10), the envelope that is the smallest deviation from constant amplitude and phase. The fine-dashed line is a solution of form (10.16), the envelope that is the smoothest deviation from constant amplitude and phase. The solid line is a solution of form (10.16), but with a discontinuity allowed at the series midpoint.

Unusual behavior, such as abrupt changes in amplitude and phase, can suggest rapid change or discontinuities in the envelope.

Two further extensions of the above treatment are useful. The first involves situations where two carrier frequencies f_1, f_2, with independent slowly varying envelopes $\mathbf{A}_1, \mathbf{A}_2$, are an appropriate model for the data. If $|f_1 - f_2| > 2pf_R$, there is minimal correlation between eigenspectra calculated using $p\pi$-prolate Slepian tapers, and the envelopes can be modeled separately. If the two carrier frequencies are more closely spaced, the envelopes should be modeled simultaneously to avoid bias. Formally, for K tapers and an N-point data series, one augments the data vector $\mathbf{y} =$

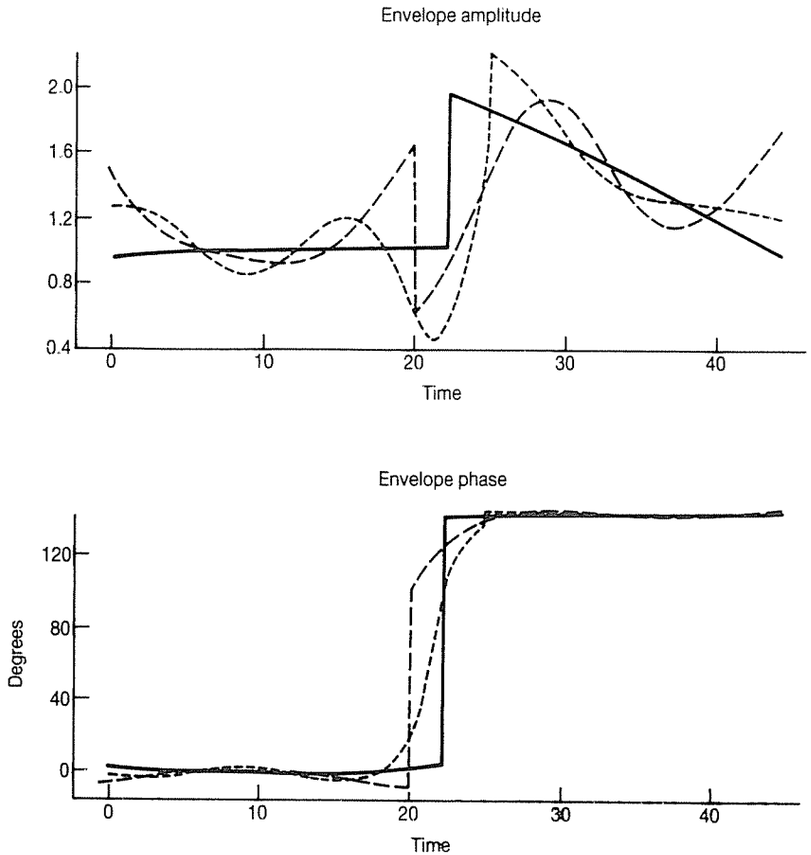

Figure 10.5 The effect of an incorrect choice of envelope discontinuity. The solid line is a solution of form (10.16) for test series B from Figure 10.4. The dashed lines are a solution of form (10.16), but with discontinuities allowed at points in the series away from the series midpoint.

$(Y_0(\hat{f}_1), \ldots, Y_{K-1}(\hat{f}_1), Y_0(\hat{f}_2), \ldots, Y_{K-1}(\hat{f}_2))$ into a complex-valued $2K$-vector, where $\hat{f}_1, \hat{f}_2$ are FFT frequencies near f_1 and f_2, respectively. One solves for a $2N$-vector $\mathbf{B} = (\mathbf{B}_1, \mathbf{B}_2)$, where $\mathbf{B}_1$ and $\mathbf{B}_2$ are estimates of $\mathbf{A}_1$ and $\mathbf{A}_2$, respectively. The first K data kernels are $2N$-vectors

$$\mathbf{g}_k = (w_1^{(k)} e^{2\pi i(\hat{f}_1 - f_1)\Delta t}, \ldots, w_N^{(k)} e^{2\pi i(\hat{f}_1 - f_1)N\Delta t}, w_1^{(k)} e^{2\pi i(\hat{f}_2 - f_1)\Delta t}, \ldots, w_N^{(k)} e^{2\pi i(\hat{f}_2 - f_1)N\Delta t}), \tag{10.20a}$$

and the second K data kernels are

$$\mathbf{g}_{K+k} = (w_1^{(k)} e^{2\pi i(\hat{f}_1 - f_2)\Delta t}, \ldots, w_N^{(k)} e^{2\pi i(\hat{f}_1 - f_2)N\Delta t}, w_1^{(k)} e^{2\pi i(\hat{f}_2 - f_2)\Delta t}, \ldots, w_N^{(k)} e^{2\pi i(\hat{f}_2 - f_2)-\Delta t}). \tag{10.20b}$$

Solutions can be obtained in a manner similar to a single-envelope inversion, with the proviso that the first-difference matrix $\mathbf{D}$ used to obtain smooth solutions must be partitioned at the midpoint of the solution vector to avoid an unwanted correlation between the endpoints of the envelope estimates $\mathbf{B}_1$ and $\mathbf{B}_2$. Note that fixed elements $\mathbf{w}_0$ used in the inversion are also $2N$-vectors in a form similar to (10.20). Care should be exercised in interpreting double-envelope inversions, because the algorithm may associate an envelope fluctuation with the wrong carrier frequency in order to satisfy the optimization condition. Roughly speaking, the likelihood of misinterpretation varies inversely with the spacing $|f_1 - f_2|$. Narrow frequency spacings also can lead to poorly conditioned kernel matrices $\mathbf{G}$.

The second extension is useful if background noise is known (or is suspected) to contribute significantly to the eigenspectrum estimates $Y_k(f)$ used as data in the above inversion schemes. A standard tactic is to allow a specified misfit to the data $S^2 = \Sigma_k (Y_k(\hat{f}_0) - \tilde{Y}_k)^2$, where $\tilde{Y}_k$ is the kth model prediction, while minimizing the penalty functional $\|\mathbf{B}\|^2$ or (10.15). Details of this method are given by Shure *et al.* (1982), in which the constrained optimization is set up with a Lagrange multiplier μ. The effect of a locally white background is roughly constant for eigenspectra for leakage-resistant Slepian tapers, so that the data misfits can be assumed to have equal variance to first order. The formal solution for real-valued kernels $\mathbf{g}_k$ is a modification of (10.12):

$$b = (\mathbf{z} \cdot \boldsymbol{\Gamma}^{-1} \cdot \mathbf{y})/(\mathbf{z} \cdot \boldsymbol{\Gamma}^{-1} \cdot \mathbf{z})$$
$$\mathbf{a} = (\boldsymbol{\Gamma} + \mu \mathbf{I})^{-1} \cdot (\mathbf{y} - b\mathbf{z}) \tag{10.21a}$$

subject to the constraint

$$\|\mathbf{y} - b\mathbf{z} - \boldsymbol{\Gamma} \cdot \mathbf{a}\|^2 = F(\mu) = S^2. \tag{10.21b}$$

The misfit variance S^2 can be chosen to represent the background noise level. In this manner the DFT of the data series near f_0 would be modeled as a quasi-periodic 'signal' embedded in a locally white background process. The value of μ consistent with (10.21) is found interatively, using the singular value decomposition of the kernel matrix $\mathbf{G} = \mathbf{V} \cdot \boldsymbol{\Psi} \cdot \mathbf{U}^T$ (Lawson and Hanson, 1974). $\mathbf{V}$ is a $K \times K$ matrix whose columns are the orthonormal left-eigenvectors $\hat{\mathbf{v}}_k$ of $\mathbf{G}$, $\mathbf{U}$ is an $N \times K$ matrix whose columns are the orthonormal right-eigenvectors $\hat{\mathbf{u}}_k$ of $\mathbf{G}$, and $\boldsymbol{\Psi} = \text{diag}\{\psi_1, \ldots, \psi_K\}$ contains the singular values of $\mathbf{G}$. The residual data vector can be decomposed $\mathbf{y} - b\mathbf{z} = \Sigma_k \mathscr{Y}_k \hat{\mathbf{v}}_k$ and the solution vector expressed as $\mathbf{a} = \Sigma_k a_k \hat{\mathbf{u}}_k$, where $a_k = \mathscr{Y}_k \psi_k / (\psi_k^2 + \mu)$. Using this decomposition, $F(\mu) = \Sigma_k \mu^2 \mathscr{Y}_k^2 / (\psi_k^2 + \mu)^2$, and the iterative solution of (10.21) using Newton's method can be performed using scalar functions. If the roughness constraint (10.15) is used as a penalty functional, the contribution of the more-oscillatory higher-order Slepian tapers to the solution will be diminished relative to that of the low-order tapers. The extension to complex-valued kernels $\mathbf{g}_k$ is straightforward.

The implementation of the above algorithms on a computer relies heavily on routines from the double-precision-complex version of the LINPACK library (Dongarra *et al.*, 1979). Routines ZQRDC and ZSVDC calculate and

manipulate the QR and SVD decompositions, respectively, of a general rectangular complex-valued matrix. The Slepian tapers $\mathbf{w}_k$ can be calculated directly from (10.4), but a more efficient method uses the fact that the tapers are also the eigenvectors of a symmetric tridiagonal matrix given by a recursion relation in eq. (10.14) of Slepian (1978). The computational burden can be decreased significantly by decimating the tapers from N to N' points and dividing the eigenspectra $Y_k(f_0)$ by the decimation factor N/N' in order to normalize the data constraints (10.9). The inaccuracy introduced by decimation is small, only affecting the solution if the kernel matrix $\mathbf{G}$ is very poorly conditioned.

10.3 Envelopes of coupled long-period seismic oscillations

The major portion of research in seismology involves the analysis of the first few wave arrivals that travel from the seismic source (earthquakes, explosions, volcanic eruptions) to the seismic receiver through the intervening Earth. These signals appear principally as transient broadband pulses – although many localities suffer extended shaking due to natural resonances in the underlying surface sediments. If the seismic source is large enough,* the ground motion excited by the source persists above the noise level long enough to enable observation of the long-period (3600 s > T > 100 s) natural resonances of the whole Earth. The spectral peaks of the whole Earth's seismic free oscillations have been studied by a variety of time-series techniques (e.g. Gilbert and Dziewonski, 1975; Buland *et al.*, 1977; Buland and Gilbert, 1978; Bolt and Brillinger, 1979; Geller and Stein, 1979; Chao and Gilbert, 1980; Dahlen, 1982; Hansen, 1982a, b; Masters and Gilbert, 1983; Giardini *et al.*, 1987; Ritzwoller *et al.*, 1986; Park *et al.*, 1987a; Lindberg and Park, 1987; Hori *et al.*, 1989; Lindberg and Thomson, 1990; Chao, 1990) – a short history of the subject can be found in Lindberg (1986).

When analysing the Earth's free oscillations, seismologists are aided by the fact that the Earth's interior is nearly 'spherical', that is, its internal properties, expressed as a function of spherical polar coordinates r, θ, ϕ, depend dominantly on the radial coordinate r. Dependence on the angular variables θ and ϕ, associated with the Earth's hydrostatic ellipticity-of-figure and lateral structure in seismic velocities (compressional and shear), density and internal friction, affect the Earth's long-period free oscillations weakly. The oscillations associated with spectral peaks in Fourier-transformed seismic data can be correlated with the oscillations of an idealized, non-rotating, spherically averaged, elastic Earth model. The equations of motion for such a body separate into distinct systems of equations that govern spheroidal and toroidal motions in the Earth. Each vibrational degree of freedom is a free oscillation 'singlet' whose angular dependence can be derived from a single fully normalized spherical harmonic $Y_l^m(\theta, \phi)$. The

* Typically, Richter-scale magnitude $M \geq 6.5$.

$2l + 1$ singlets with azimuthal orders $m = -l, -l + 1, \ldots, l - 1, l$ that share angular degree l and the same dependence on radius r form a 'multiplet' with degenerate frequency f. Spheroidal-motion multiplets are denoted by ${}_nS_l$, where n indicates the radial overtone number. Toroidal-motion multiplets are denoted by ${}_nT_l$. Using Rayleigh's variational principle (Aki and Richards, 1980), a model of weak spherically averaged anelasticity can be used to calculate the quality factor, or Q, of each multiplet oscillation. Each vibrational singlet is represented by a vector-valued function $\mathbf{s}_k(\mathbf{r})$, defined at positions $\mathbf{r}$ within the Earth, which describes the particle displacement associated with the oscillation. The response $\mathbf{u}(\mathbf{r}, t)$ of a spherically symmetric, nonrotating Earth to a seismic event at $t = 0$ with step-function time dependence can be expressed as an infinite sum of vibrational free oscillations $s_k(\mathbf{r})$ (Gilbert and Dziewonski, 1975),

$$\mathbf{u}(\mathbf{r}, t) = \sum_{k=1}^{\infty} \mathbf{s}_k(\mathbf{r}) \aleph_k (\cos \omega_k t e^{-\alpha_k t} - 1) H(t) \tag{10.22}$$

where $\aleph_k$ is the excitation scalar for the kth singlet, $\omega_k = 2\pi f_k$ is the radial frequency of oscillation, $H(t)$ is the stepfunction and $\alpha_k = \omega_k / 2Q_k$, where Q_k is the quality factor of the kth singlet. If we neglect internal-wave motions in the liquid outer core, the frequencies $\omega_k \to \infty$ as $k \to \infty$.

The effect of deviations from a spherical reference model on the free oscillations can be treated with perturbation theory – see Park (1988) for a review. On a weakly aspherical, slowly rotating Earth, the singlets of a spherical reference Earth model couple and hybridize, and their frequencies split into a cluster in narrow bands in the neighborhood of the spherical-Earth multiplet frequencies. An analogy can be made between coupled-mode singlet frequencies and splitting of the electron energy states for atoms and molecules, as the matrix equations that govern splitting have similar structure. For some multiplets, the individual singlet oscillations are resolvable and can be 'stacked' using a global array (e.g. Buland *et al.*, 1977; Ritzwoller *et al.*, 1986). Most often the singlets are unresolvable and a free oscillation multiplet is modeled by $u(t) = \Re\{A(t)e^{-2\pi i f_0 t}\}$, where $A(t)$ is a slowly varying complex-valued envelope of a cosinusoid with carrier frequency f_0. The carrier frequency f_0 is typically, but not always, the spherical-Earth frequency of the multiplet.

The slow variation of $A(t)$ is equivalent to narrow-band concentration of energy in its Fourier transform $\bar{A}(f)$ about $f = 0$. Attempts to extract information from $A(t)$ pertaining to Earth asphericity have taken the form of narrow-band integrals of $\bar{A}(f)$ (the 'multiplet moments' of Jordan (1978)) and Born-series expansions of $A(t)$ (Woodhouse, 1983; Smith and Masters, 1989). However, the potential for complex coupling interaction, such as that between spheroidal and toroidal multiplets due to rotation (Masters *et al.*, 1983; Park, 1986), makes a direct estimate of $A(t)$ useful in some situations. Narrow-band filtering is an option for retrieving $A(t)$ from long-period seismic records, e.g. Geller and Stein (1979), Hansen (1982a, b). However, an extremely long filter would be necessary to isolate the behavior of most free oscillation spectral peaks, making the onset of the oscillation difficult to resolve.

It is conventional to distinguish 'self-coupling' among the $2l+1$ degenerate singlets within an isolated multiplet ${}_nS_l$ or ${}_nT_l$ and the more general coupling between singlets belonging to distinct multiplets. The perturbation of the initial amplitude and phase of the multiplet envelope $A(t)$ caused by self-coupling is negligible. The coupling of a multiplet with nearby multiplets will perturb its initial amplitude (Park, 1987), and coupling with multiplets that possess different Q will perturb the initial phase of the complex-valued oscillation envelope. To see this, consider the coupling of two oscillation singlets $\mathbf{s}_1, \mathbf{s}_2$ with radial frequencies ω_1, ω_2, quality factors Q_1 and Q_2 and cross-coupling interaction term ε. Assume the oscillations are unit-normalized, ε is real-valued, and neglect other coupling interaction to simplify the algebra. The hybrid singlets and their oscillation frequencies are found from the eigenvectors and eigenvalues of the matrix

$$\begin{bmatrix} \omega_1^2(1-\mathrm{i}Q_1^{-1}) & \varepsilon \\ \varepsilon & \omega_2^2(1-\mathrm{i}Q_2^{-1}) \end{bmatrix}. \tag{10.23}$$

If we define

$$\begin{aligned} \Lambda &= (\omega_1^2(1-\mathrm{i}Q_1^{-1}) + \omega_2^2(1-\mathrm{i}Q_2^{-1}))/2 \\ \gamma &= (\omega_1^2(1-\mathrm{i}Q_1^{-1}) - \omega_2^2(1-\mathrm{i}Q_2^{-1}))/2\varepsilon, \end{aligned} \tag{10.24}$$

the hybrid eigenfrequencies satisfy $\tilde{\omega}_\pm^2 = \Lambda \pm \sqrt{(\gamma^2+1)}$. The hybrid singlets and excitation scalars are

$$\begin{aligned} \tilde{\mathbf{s}}_\pm &= \mathbf{s}_1 + (\gamma \pm \sqrt{(\gamma^2+1)})\mathbf{s}_2 \\ \tilde{\aleph}_\pm &= (\aleph_1 + (\gamma \pm \sqrt{(\gamma^2+1)})\aleph_2)/\eta_\pm, \end{aligned} \tag{10.25}$$

where $\eta_\pm = 2(\gamma^2 + 1 \pm \gamma\sqrt{(\gamma^2+1)})$. In general, the hybrid singlets $\tilde{\mathbf{s}}_\pm$ will be excited with initial phase $\phi_0 \neq 0°$ or $180°$. If the frequency difference $\Re\,\Delta\tilde{\omega} = \Re(\tilde{\omega}_1 - \tilde{\omega}_2)$ is too small to resolve with a given seismic record length, the observed oscillation envelope is the sum of $\tilde{\mathbf{s}}_1$ and $\tilde{\mathbf{s}}_2$. The amplitude $|A(t)|$ of the envelope will beat with period $2\pi/\Re\,\Delta\tilde{\omega}$. The beating will weaken with time as the oscillation with lower Q decays relative to its partner. A beating envelope may be observed even if coupling is absent, if both $\mathbf{s}_1$ and $\mathbf{s}_2$ are excited and are observed on the same component of ground motion.

Coupled seismic free oscillations can be observed on three separate ground-motion components, which aids the detection of coupling between spheroidal and toroidal multiplets. The east and north horizontal ground motion, as measured by the seismometer, can be rotated into radial (R) and transverse (T) components, parallel and perpendicular, respectively, to the great circle connecting source and receiver on the Earth's surface. Toroidal motion is absent from the vertical component and, for $l \gg 1$, only weakly present on the radial component of horizontal ground motion. Likewise, for $l \gg 1$, spheroidal motion is only weakly present on the transverse horizontal component. Therefore beating observed in the oscillation envelope, especially on the vertical component, can be taken as strong evidence of mixed-type modal coupling. In particular, we expect to observe a behavior common to all weakly coupled systems: motion excited on, say, the toroidal component

of motion should rotate slowly onto the spheroidal motion component and back again. The strongest coupling observed between spheroidal and toroidal multiplets is caused by the Coriolis force associated with the Earth's rotation. The strength of mixed-type rotational coupling varies with the latitude of the source–receiver great-circle pole (Park, 1986), with strongest interaction on polar (north–south) propagation paths.

The 5/23/89 Macquarie Islands earthquake is nearly ideal for the study of spheroidal–toroidal coupling. The earthquake is one of the largest (surface-wave magnitude $M_s = 8{\cdot}1$, seismic moment $M_0 \approx 2{\cdot}0 \times 10^{21}$ N m) events to occur since the installation of digital seismic networks (Ekstrom and Romanowicz, 1990; Braunmiller and Nabelek, 1990), and has an unusually short inferred rupture duration (Tichelaar and Ruff, 1990; Houston, 1990). The epicentre is at high latitude (52·5°S), so that all propagation paths are more polar than equatorial in orientation. The source geometry is almost pure strike-slip (fault strike $\approx 35°$ west of north, right-lateral motion), which enhances toroidal-motion excitation.

Horizontal components from most stations are fairly noisy at long periods, except from a handful of new and recently upgraded stations with quiet sites and modern broadband-response seismometers. Horizontal-component data from such stations can have signal-to-noise nearly equal to that of the vertical component. Strong mixed-type rotational coupling is predicted from synthetic seismograms for the Macquarie event. The behavior of this interaction is evident in smooth-envelope inversions of hybrid Ts–St multiplet pairs. Figures 10.6 and 10.7 show spectrum estimates and smooth envelope inversions for the multiplet pair ${}_0S_{11}$–${}_0T_{12}$ on station PAS (Pasadena, California), part of the Global Seismic Network operated by the US Geological Survey and the Incorporated Research Institutions for Seismology (IRIS). The data analyzed is collected on the VP-channel of this seismometer, which samples ground motion at $0{\cdot}1\ \mathrm{s}^{-1}$, low-passed and decimated to $\Delta t = 40$ s. Figure 10.6 shows 'high-resolution' spectra (Thomson, 1982), calculated from 40-hour records with five 3π-prolate Slepian tapers appropriate for $0{\cdot}9Q$-cycles of decay and $\eta = 0$. The decay rate is chosen to be larger than that experienced by the modes ${}_0S_{10}$, ${}_0S_{11}$ and ${}_0S_{12}$, but less than the decay experienced by the modes ${}_0T_{11}$, ${}_0T_{12}$ and ${}_0T_{13}$. The frequency band shown is a cross-over between the ${}_0S_l$ and ${}_0T_{l+1}$ dispersion branches, for which the angular selection rules for Coriolis-force coupling predict interaction.

Results of smooth-envelope inversions for the V (vertical), R and T ground motion components of the spectral peaks corresponding to ${}_0S_{11}$–${}_0T_{12}$ are shown in Figure 10.7. The complex-valued envelopes are corrected for instrument response, and are given in units of ground displacement. The envelopes are boosted by $0{\cdot}9Q$-cycles of exponential growth to appear relatively decay-free for display, so the displacement units are accurate only at $t = 0$ h. Envelopes inferred for the vertical and radial components share a minimum at $t = 22$ h, suffering a phase shift approaching $180°$. The transverse-component envelope varies oppositely, with a maximum near $t = 23$ h and minima where the other components are larger. The phase of the envelopes jumps by $\approx 180°$ where the envelope amplitude is close to zero. The phase drift suggests that the chosen carrier frequency $f_0 = 1{\cdot}860$ mHz differs slightly

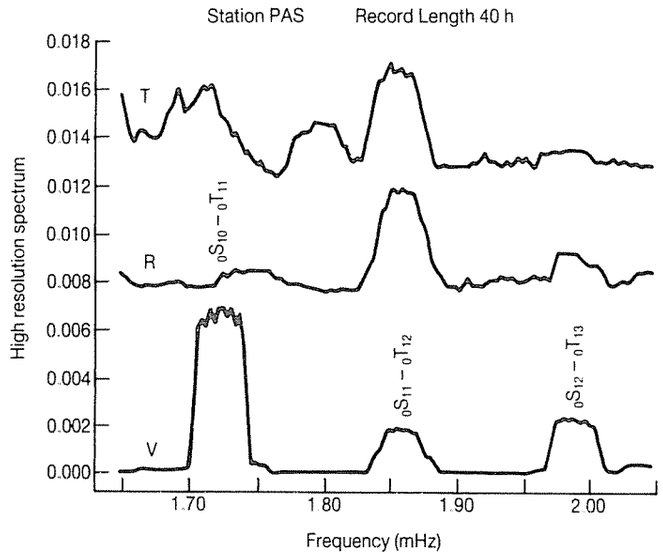

Figure 10.6 High-resolution spectrum estimates using long-period seismic data from station PAS (Pasadena, California) recorded after the $M_S = 8{\cdot}1$ Macquarie Ridge earthquake of 23 May 1989. Vertical (V), radial–horizontal (R) and transverse–horizontal (T) spectrum estimates were computed with five 3π-prolate Slepian tapers with noise-weighting $\eta = 0$ and exponential-decay parameter $\beta = 0{\cdot}9$. Peaks are indicated that correspond to spheroidal–toroidal free oscillation multiplet pairs known to couple through rotational Coriolis force.

from the dominant frequency in the data. The overall behavior is consistent with the simple coupled-oscillation model discussed above, in which vibrational motion alternates slowly between spheroidal and toroidal ground motion. Observed in a narrow frequency passband at the receiver site, ground motion tends to rotate like a Foucault pendulum – although the period of this rotation depends on the Earth's interior properties and not simply on latitude. Figure 10.8 shows the envelope estimates for multiplet pairs ${}_0S_{31}-{}_0T_{30}$ and ${}_0S_{37}-{}_0T_{35}$ for VP-channel seismograms collected by stations WMQ (Urumchi, China) and KMI (Kunming, China), respectively, in the Chinese Digital Seismic Network. Analysis is similar to that applied to the PAS record, though the more-rapid decay of the higher-frequency oscillations limits analysis to 20-hour records. Angular selection rules suggest that ${}_0S_{31}-{}_0T_{30}$ is sensitive to Coriolis-force coupling, and is supported by the observed rotation of vibration motion in the narrow passband around the carrier frequency $f_0 = 3{\cdot}90$ mHz. Coriolis-force coupling is forbidden for ${}_0S_{37}-{}_0T_{35}$, so the likely cause of the apparent rotation of vibrational motion between the radial and transverse components is related to lateral structure in the Earth's internal properties.

The detailed structure of long-period seismic motion may help constrain internal variations in Earth properties that govern long-period scattering in

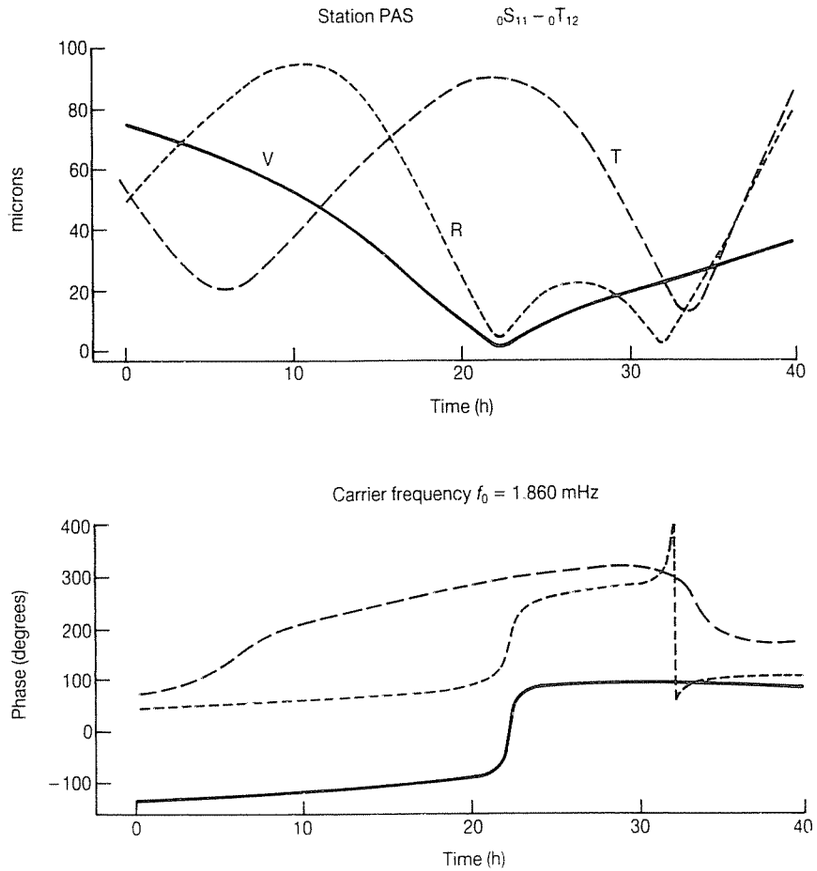

Figure 10.7 Smooth-envelope estimates for PAS data at a carrier frequency appropriate for the free oscillations ${}_0S_{11}$ ($f = 1{\cdot}8611$ mHz, $Q = 340$) and ${}_0T_{12}$ ($f = 1{\cdot}8599$ mHz, $Q = 178$). Frequencies are obtained from spherically averaged Earth model 1066A (Gilbert and Dziewonski, 1975) and attenuation rates from the model of Masters and Gilbert (1983). Plots indicate the smoothest deviation from a simple decaying sinusoid with $0{\cdot}9Q$-cycles of decay ($Q \approx 298$) in the duration of the data record. Decay is removed from the envelopes for display.

the Earth. The particle-motion associated with free-oscillation multiplets varies on the Earth's surface according to associated spherical harmonics $Y_l^m(\theta, \phi)$, $-l \leqslant m \leqslant l$. Therefore it should be possible to extend the single-station analysis presented here to a multiple-station inversion using a global network of seismometers. Observations of envelope fluctuations for spheroidal–toroidal multiplet pairs may be useful in this regard, as modeling studies suggest that source–receiver paths on which mixed-type coupling is strong are associated with considerable lateral structure and/or anisotropy

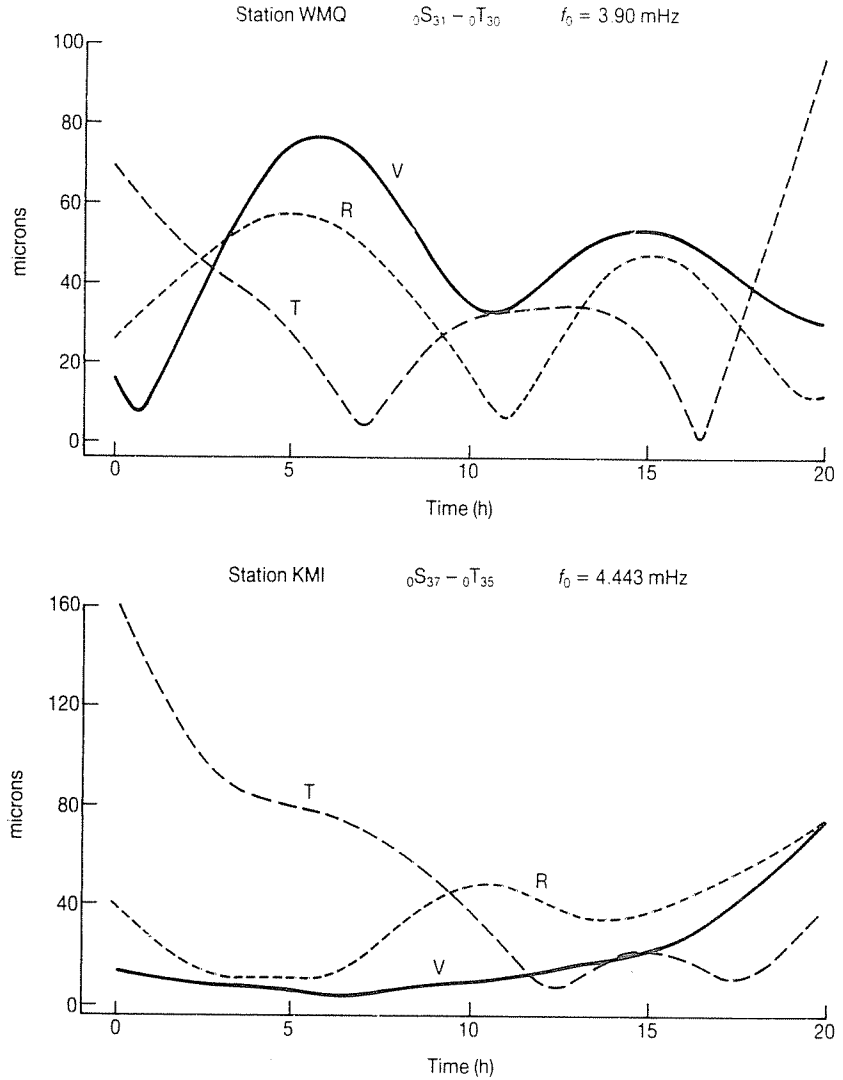

Figure 10.8 Smooth-envelope estimates using long-period seismic data recorded after the $M_S = 8{\cdot}1$ Macquarie Ridge earthquake of 23 May 1989. Vertical (V), radial–horizontal (R) and transverse–horizontal (T) spectrum estimates were computed with five 3π-prolate Slepian tapers with noise-weighting $\eta = 0$ and exponential-decay parameter $\beta = 1{\cdot}5$. Decay is removed from the envelopes for display. (a) Envelopes for data from station WMQ (Urumchi, China) at a carrier frequency appropriate for the free oscillations ${}_0S_{31}$ ($f = 3{\cdot}9031$ mHz, $Q = 198$) and ${}_0T_{30}$ ($f = 3{\cdot}8834$ mHz, $Q = 133$). Plots indicate the smoothest deviation from a simple decaying sinusoid with $1{\cdot}5Q$-cycles of decay ($Q \approx 187$) in the duration of the data record. (b) Envelopes for data from station KMI (Kunming, China) at a carrier frequency appropriate for the free oscillations ${}_0S_{37}$ ($f = 4{\cdot}4382$ mHz, $Q = 172$) and ${}_0T_{35}$ ($f = 4{\cdot}4324$ mHz, $Q = 129$). Plots indicate the smoothest deviation from a simple decaying sinusoid with $1{\cdot}7Q$-cycles of decay ($Q \approx 188$) in the duration of the data record.

in seismic velocity. Significant observational hurdles exist, not the least of which is that the number of sufficiently-low-noise long-period seismograms is limited by the number of large earthquakes ($M \geqslant 7{\cdot}5$ is best) and the number of high-quality seismic stations. Over time both limitations should recede. Contamination of envelope inversions by neighboring multiplets (e.g. fundamental-mode envelope observations contaminated by overtones) is a potential problem in all records. For instance, the local maximum at $t \approx 10$ h in the radial-component envelope appears related to the transfer of vibrational motion from the T-component, but the likely cause of the growth in the R- and V-envelopes at the record's end is contamination by a relatively high-Q spheroidal overtone multiplet. The latter's weak excitation by the earthquake source is compensated, after 20 h, by greater resistance to exponential decay. With these caveats in hand, smooth-envelope analyses of free oscillation may prove a useful tool in the investigation of the Earth's interior.

10.4 Orbital quasi-periodicities in paleoclimate data

Study of Pleistocene and Pliocene deep-sea cores has demonstrated the sensitivity of the Earth's climate system to small variations in insolation caused by cyclic changes in the geometry of the Earth's orbit and tilt (Hays *et al.*, 1976; Imbrie *et al.*, 1984; Berger, 1988). Cycles have been observed in $\delta^{18}O$ measurements, which record variations in global ice volume and ocean temperature, $\delta^{13}C$ measurements, a proxy for the supply of nutrients to the deep ocean, and sea–surface temperatures as inferred from foraminiferal assemblages. Rhythmic sedimentary oscillations of parameters related to global climate continue into the more remote geologic past, suggesting a long history of orbital modulation of Earth climate (Herbert and Fischer, 1986; Olsen, 1986). The solar system celestial mechanics problem is quasi-periodic, and numerical solutions are available that are reliable for the last 1–2 My (Berger, 1984; Bretagnon, 1984). The astronomical forcing series that governs long-term insolation variation consists of several groups of closely spaced lines near 413, 126, 96, 41, and 19–23 ky period (Berger, 1978).

Significant anomalies in the solar insolation received by the Earth are associated with the Earth's precession (19–23 ky) and obliquity (41 ky) cycles. Studies with atmospheric global circulation models suggest that these insolation variations can cause profound variations in average Earth climate (Kutzbach and Guetter, 1986; Prell and Kutzbach, 1987). The longer-period eccentricity cycles (96, 126, 413 ky and longer) are associated with much smaller insolation anomalies, but appear to dominate oxygen-isotope records of ice-sheet growth since roughly 1 Ma, as well as climate proxy variables from certain Cretaceous sequences (Herbert and Fischer, 1986; Park and Herbert, 1987). The eccentricity of the Earth's orbit modulates the seasonal insolation anomaly associated with the Earth's precession, so that the eccentricity cycle is the envelope of the precession cycle. Therefore the presence

of eccentricity cycles in older sediments may be caused in part by the smearing of thin precession cycles by bioturbation or diagenesis. This explanation is untenable in the late Pleistocene, and the presence of a 100 ky ice-age cycle has been attributed to other factors in the Earth's climate system, such as a nonlinear response to precession and obliquity forcing (Birchfield and Weertman, 1978) or an internal oscillation unrelated to Milankovitch forcing (Saltzman and Sutera, 1984; Maasch and Saltzman, 1990).

Our understanding of the 100 ky ice-age cycle is hampered by the difficulty of modeling its evolution through time, particularly the timing and nature of its onset, thought to have occurred sometime in the interval 0·5–1·0 Ma. Was the onset of the 100 ky cycle gradual or sudden? A sudden onset would be characteristic of a bifurcation in a nonlinear system (Maasch and Saltzman, 1990), and would suggest the existence of a fundamental instability in the terrestrial climate system. A gradual increase in ice-age cycle intensity could, by contrast, suggest a shift in an otherwise stable climate regime or the steady growth of an unstable oscillation. Maasch (1988) analyzed several $\delta^{18}O$ and proxy sea surface temperature records for the Pleistocene, and found evidence for a sudden jump in the mean (towards greater average ice mass and cooler average global temperatures) at 0·9 Ma. Ruddiman *et al.* (1989) and Raymo *et al.* (1989) analyzed climate proxy data from DSDP cores 607 and 609, both from the North Atlantic Ocean, to study cyclic climate response. Ruddiman *et al.* (1989) applied bandpass filters to the data series to study the evolution of the 100 ky ice-age near the inferred mid-Pleistocene climate transition. This analysis suggested an increase in amplitude between 0·9 and 0·4 Ma, with the most rapid increase between 0·7 and 0·6 Ma.

Narrow-band filters cannot model discontinuities in the envelope of a quasi-periodic signal, and so are of little help in discriminating between sudden and gradual onset of the 100 ky ice-age cycle. The multi-taper envelope estimation procedure outlined in this chapter can model envelope discontinuities, and offer some aid in this respect. It must be stressed, however, that the technique cannot by itself discriminate between continuous and discontinuous models for the 100 ky cycle, since models of both types can be constructed that fit the spectral 'data' exactly. Rather, the analyst must use other criteria in choosing to accept or reject different models. We demonstrate such use of the algorithm using the 'Site 607' $\delta^{18}O$ data series analyzed by Ruddiman *et al.* (1989) and Raymo *et al.* (1989), a composite of data from sediments drilled at DSDP Site 607 and two other piston cores. This data set extends from the present through the Pleistocene into the Pliocene, and is inferred to represent roughly 2·7 My of deposition. The $\delta^{18}O$ data is sampled at an average spacing of 15 cm, corresponding to an average time spacing of 3·4 ky. We used the time scale derived by Ruddiman *et al.* (1989) by tuning the series against astronomical obliquity and precession variations. The unevenly spaced data set was interpolated with a cubic spline to obtain an evenly spaced series ($\Delta t = 2$ ky) for analysis. A small amount of misfit to the data was allowed when constructing the cubic spline interpolator (Reinsch, 1967), in order to avoid spurious oscillations in the neighborhood of a handful of closely spaced pairs of data points.

Multi-taper spectrum estimation was performed on the Site 607 record and the corresponding 2·7 My segment of the astronomical eccentricity series (Berger, 1978) using seven 4π-prolate Slepian tapers. Following standard convention, the sign of the $\delta^{18}O$ data was reversed so that lighter isotopic values (i.e. decreased ice volume) correlate with maxima in orbital eccentricity. The spectrum of the astronomical eccentricity series (Figure 10.9) is dominated by quasi-periodic oscillations at 96, 126 and 413 ky (10·4, 7·94 and 2·42 cyc/My, respectively). The complex-valued envelopes of the 96 and 126 ky signals (Figure 10.10), modeled simultaneously with seven 4π-prolate Slepian tapers, a constant-amplitude fixed element and roughness penalty (10.15), vary in tandem, sharing a minimum and a phase jump near 2 Ma. The high-resolution multi-taper spectrum estimate of the 'Site 607' series (Figure 10.11) shows a peak centered near 10·4 cyc/My, with a shoulder at lower frequency. Statistical tests for phase-coherence (Thomson, 1982; Park and Herbert, 1987) show weak peaks (<99% confidence for nonrandomness) near 96 and 126 ky period, as well as periods not associated with primary Milankovitch cycles. When this peak and shoulder are modeled in terms of envelopes of oscillations with carrier frequencies 7·94 and 10·4 cyc/My (Figure 10.12), poor correlation with the astronomical signal is found before 1 Ma – note the lack of a clear minimum near 2·0 Ma. The phase of both envelopes agrees fairly well with the astronomical series for ages less than 1 Ma. The growth of envelope amplitude for the 126 ky quasi-period appears

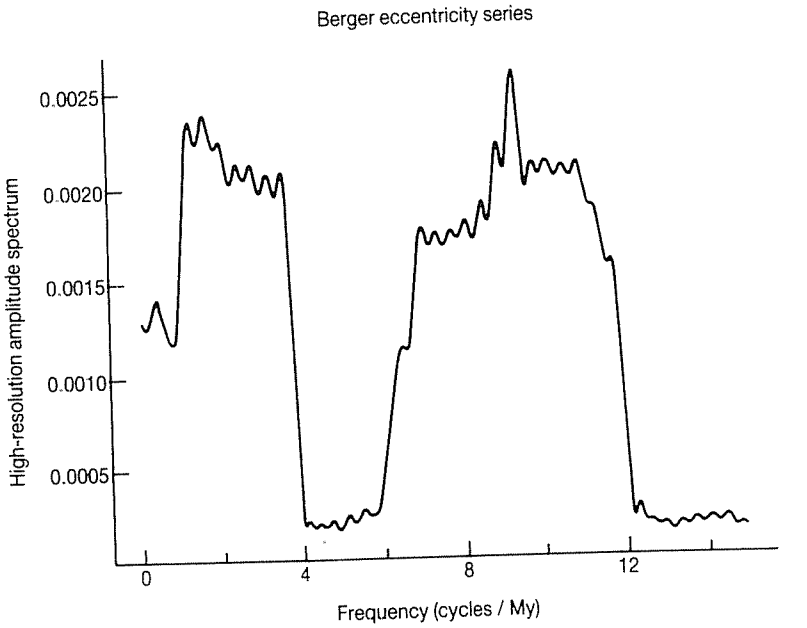

Figure 10.9 High-resolution spectrum estimate of the astronomical eccentricity series from Berger (1978), evaluated from the present to 2·7 Ma. Seven 4π-prolate Slepian tapers were used.

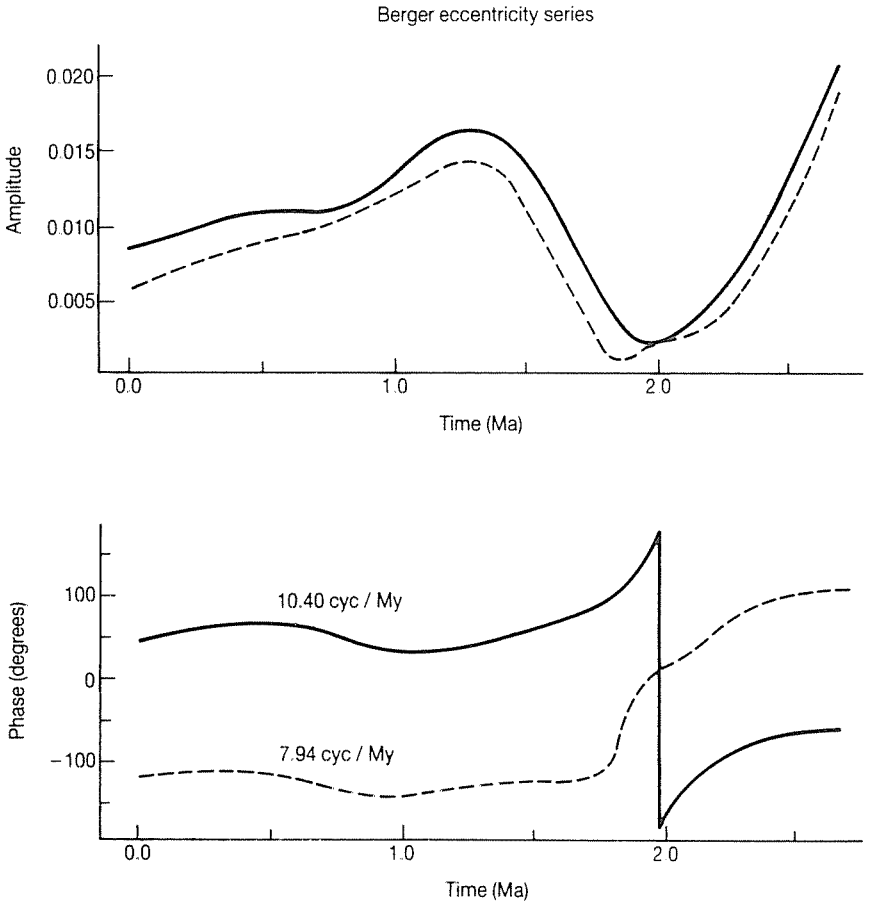

Figure 10.10 Envelope models for the quasi-periodic signal centered at carrier frequencies 7·94 and 10·4 cyc/My, using the astronomical eccentricity series. Seven 4π-prolate Slepian tapers were used, with the roughness penalty function (10.15) and a constant-amplitude fixed element.

to start at 1·25 Ma. This growth is dwarfed by the growth of the 96 ky envelope amplitude, which rises from zero at 1·0 Ma to a maximum at 0·45 Ma, then declines. The behavior of the 96 ky envelope is broadly consistent with that reported by Ruddiman *et al.* (1989) for the 100 ky bandpass. Multi-taper envelope estimation allows the simultaneous modeling of the envelope of signal at the nearby 126 ky eccentricity period.

Although the above smooth-envelope inversion suggests a gradual increase in the 100 ky cycle, abrupt onsets are also consistent with the data. Figure 10.13 shows results of smooth-envelope inversions at $f_0 = 10{\cdot}4$ cyc/My with discontinuities allowed at 0·7, 0·85, and 1·0 Ma. A discontinuity allowed at 1·0 Ma leads to an envelope similar to that shown in Figure 10.12. A discontinuity allowed at 0·7 Ma leads to an envelope with a sharp amplitude maximum at the discontinuity. Note that the phase of this envelope (coarse-dashed line in the figure) attempts to match phase across the discontinuity, suggesting that some 100 ky signal with phase close to that of the astronomical cycle exists at ages greater than 0·7 Ma. By contrast, a discontinuity allowed at 0·85 Ma leads to an envelope with roughly constant amplitude at ages younger than 0·85 Ma, and no anomalous deviation in phase at times older than the discontinuity. Based on this comparison, a sudden onset of the ice-age cycle at 0·85 Ma, but not significantly earlier or later, appears a reasonable model for the narrow-band 100 ky signal.

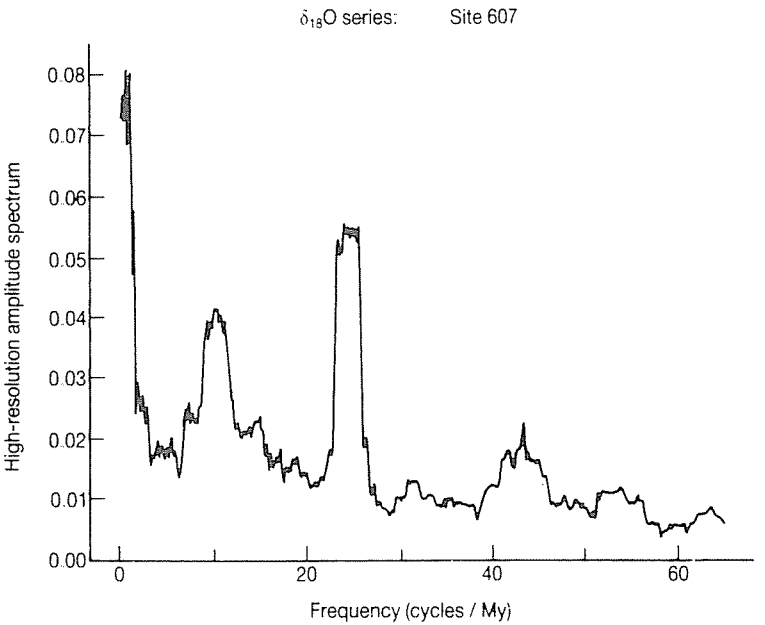

Figure 10.11 High-resolution spectrum estimate of the Site 607 $\delta^{18}O$ data series reported by Ruddiman *et al.* (1989) and Raymo *et al.* (1989), evaluated from the present to 2·7 Ma. Seven 4π-prolate Slepian tapers were used.

Firmer conclusions about the evolution of the Pleistocene ice-age cycle cannot be reached without a more thorough analysis of this and other climate proxy records. Such an analysis is beyond the scope of the present chapter. We note that time-scale uncertainties in paleoclimate time series create difficulties in interpretation, especially for the quasi-periods used to tune the time scale. For example, smooth envelope inversion for the obliquity signal ($f_0 = 24{\cdot}35$ cyc/My) suggests amplitude variations by a factor of two, with a maximum between 0·9 and 1·5 Ma. Phase variations for this envelope, however, have been suppressed by the use of obliquity as a tuning tool. The time scale given by Ruddiman *et al.* (1989) was engineered to minimize phase fluctuations in the obliquity signal, using an assumed 10 ky phase lag between obliquity and glacial maxima.

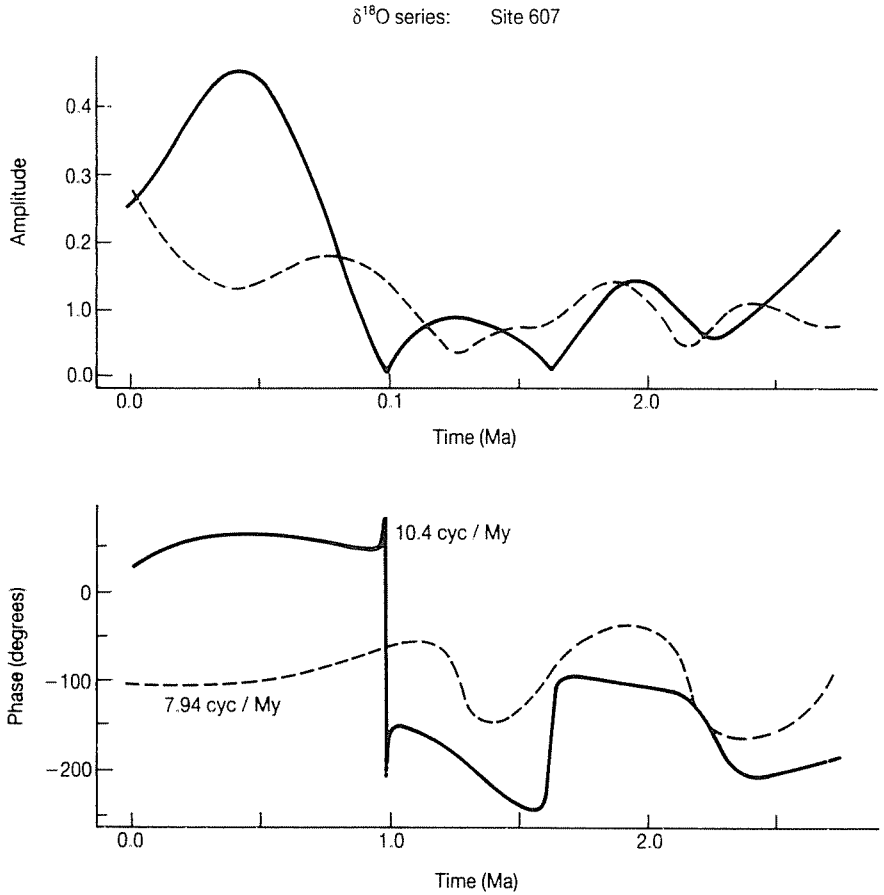

Figure 10.12 Envelope models for the quasi-periodic signal centered at carrier frequencies 7·94 and 10·4 cyc/My, using the Site 607 δ^{18}O data series. Seven 4π-prolate Slepian tapers were used, with the roughness penalty function (10.15) and a constant-amplitude fixed element.

10.5 Summary

It is often useful to model the time-evolution, or envelope, or quasi-periodic signals in geological and geophysical time series. Multi-taper envelope estimation is a generalization of narrow-bandpass filtering which allows *a priori* constraints to be imposed on the envelope of such a signal, while requiring that the amplitude and phase of the complex-valued envelope be consistent with spectral information in the neighborhood of a carrier frequency f_0. In particular, we use the eigenspectrum estimates $Y_k(f_0)$ (complex-valued), obtained via the discrete Fourier transform of the data multiplied by one of a set of K $p\pi$-prolate Slepian tapers, as 'data' in a linear inverse problem to construct models for the complex-valued envelope. The Slepian tapers serve

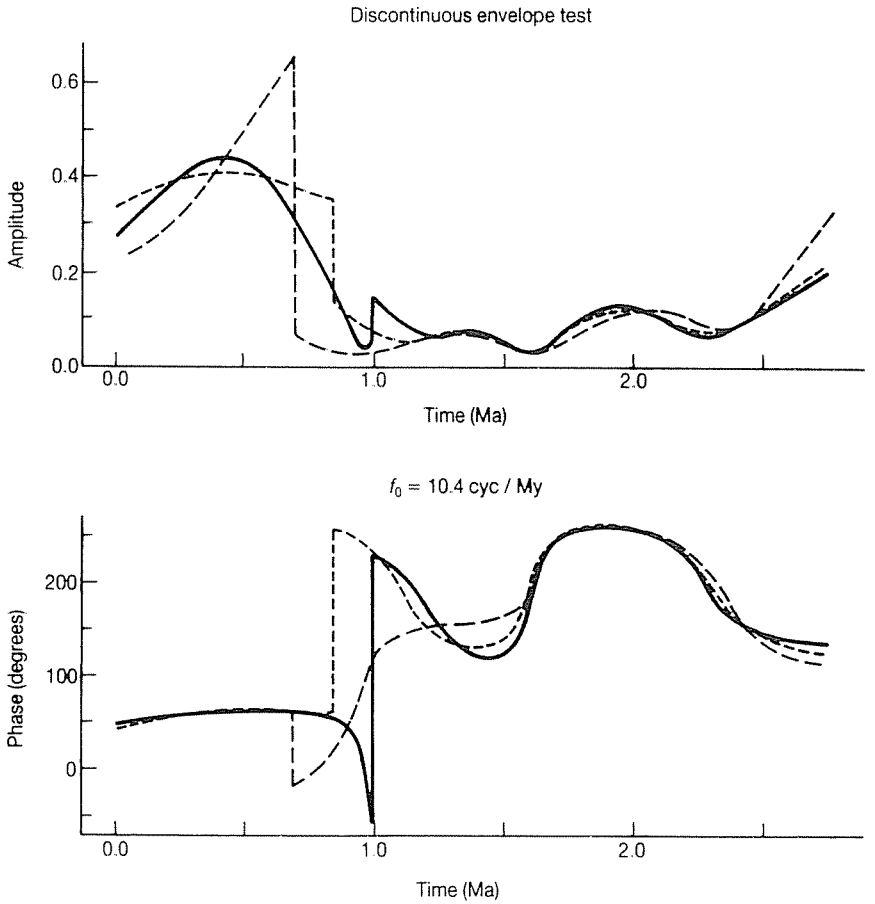

Figure 10.13 Envelope models for carrier frequency $f_0 = 10{\cdot}4$ cyc/My, using the Site 607 δ^{18}O data series. Seven 4π-prolate Slepian tapers were used, with a constant-amplitude fixed element. A roughness penalty is applied everywhere save a single point in time, where a discontinuous jump in the envelope is allowed. Break points shown are 1·0 Ma (solid line), 0·85 Ma (fine-dashed line) and 0·7 Ma (coarse-dashed line).

as kernel functions, or data representers, in the inversion. The Slepian tapers are orthogonal when summed over the series, so that, for locally white data processes, the eigenspectra are statistically uncorrelated. This orthogonality carries over into the manner that the eigenspectra $Y_k(f_0)$ sample the frequency-domain representation $\bar{A}(f)$ of the quasi-periodic signal over the frequency range $[f_0 - pf_R, f_0 + pf_R]$, where $f_R = 1/T$ and T is the duration of the time series. Therefore spectrum estimates using a set of Slepian tapers offer a natural and efficient way to investigate the narrow-band behavior of $\bar{A}(f)$. Envelopes constructed as linear combinations of Slepian tapers can represent the envelope near the ends of the time series, whereas the use of

M-point bandpass filters discards $M-1$ data points from each end of the series.

All linear inverse problems with finite data have non-unique solutions, but unique models can be constructed that minimize a suitably defined penalty function. A roughness penalty of the form (10.15) is a plausible constraint, as it tends to preserve the bandlimited nature of a quasi-periodic signal. Abrupt changes in an otherwise smoothly varying envelope can be modeled by a suitable modification of the roughness penalty function. Other constraints, data misfit tolerance, and additional model parameters (e.g. a second carrier frequency) can be incorporated into the inverse problem. Discrimination between envelope models often involves criteria specific to the analyzed data set. However, spectral information from outside the narrow band centered on f_0 sampled by the Slepian tapers may be useful in constraining the problem if a suitable case can be made that such spectral information is not contaminated by signals with dominant frequency $f \neq f_0$.

Acknowledgements

I thank Robert Parker for providing a draft copy of his unfinished text on inverse theory. I thank the staff at the IRIS DMC for help in accessing data from the Macquarie Ridge earthquake. I thank Kirk Maasch for helpful comments and for providing a computer file of the Site 607 $\delta^{18}O$ data series, which was provided to him by M.E. Raymo, to whom I also express gratitude. This work has been supported by NSF grant EAR-8657206.

References

Aki, K. and Richards, P.G. (1980). *Quantitative Seismology*, Vol. 1. Freeman, San Francisco.

Berger, A. (1978). A simple algorithm to compute long-term variations of daily or monthly isolation. *Inst. Astron. Geophys. G. Lemaitre*, Contrib. 18, 17 pp.

Berger, A. (1984). Accuracy and frequency stability of the earth's orbital elements during the Quaternary. In *Milankovitch and Climate*, Part 1, Berger, A., Imbrie, J., Hays, J., Kukla, G., and Saltzman, B. (eds). D. Reidel, Hingham, Mass.

Berger, A. (1988). Milankovitch theory and climate. *Rev. Geophys.*, **26**, 624–57.

Birchfield, G.E. and Weertman, J. (1978). A note on the spectral response of a model continental ice sheet. *J. Geophys. Res.*, **83**, 4123–5.

Bolt, B. and Brillinger, D.R. (1979). Estimation of uncertainties in eigenspectral estimates from decaying geophysical time series. *Geophys. J. Roy. Astron. Soc.*, **59**, 593–603.

Braunmiller, J. and Nabelek, J. (1990). Rupture process of the Macquarie Ridge earthquake of May 23, 1989. *Geophys. Res. Lett.*, **17**, 1017–20.

Bretagnon, P. (1984). Accuracy of long-term planetary theory. In *Milankovitch and Climate*, Part 1, Berger, A., Imbrie, J., Hays, J., Kukla, G., and Saltzman, B. (eds), D. Reidel, Hingham, Mass.

Buland, R. and Gilbert, F. (1978). Improved resolution of complex eigenfrequencies in analytically continued seismic spectra. *Geophys. J. Roy. Astron. Soc.*, **52**, 457–70.

Buland, R., Berger, J., and Gilbert, F. (1977). Observations from the IDA network of attenuation and splitting during a recent earthquake. *Nature*, **277**, 358–62.

Chao, B.F. (1990). Commentary on 'A new method of spectral analysis and its application to the Earth's free oscillations: The "Sompi" method'. *J. Geophys. Res.*, **95**, 19 789–90.

Chao, B.F. and Gilbert, F. (1980). Autoregressive estimation of complex eigenfrequencies in low frequency seismic spectra. *Geophys. J. Roy. Astron. Soc.*, **63**, 641–57.

Constable, S.C., Parker, R.L., and Constable, C.G. (1987). Occam's inversion: A practical algorithm for generating smooth models from electromagnetic sounding data. *Geophysics*, **52**, 289–300.

Dahlen, F.A. (1982). The effect of data windows on the estimation of free oscillation parameters. *Geophys. J. Roy. Astron. Soc.*, **69**, 537–49.

Dongarra, J.J., Moler, C.B., Bunch, J.R., and Stewart, G.W. (1979). *LINPACK User's Guide*, Society for Industrial and Applied Mathematics, Philadelphia.

Ekstrom, G. and Romanowicz, B. (1990). The 23 May, 1989 Macquarie Ridge earthquake: A very broad band analysis. *Geophys. Res. Lett.*, **17**, 993–6.

Geller, R.J. and Stein, S. (1979). Time domain attenuation measurements for fundamental spheroidal modes ($_0S_6$–$_0S_{28}$) for the 1977 Indonesian Earthquake. *Bull. Seism. Soc. Amer.*, **69**, 1671–92.

Giardini, D., Xi, X.-D., and Woodhouse, J.H. (1987). Three dimensional structure of the Earth from splitting in free oscillation spectra. *Nature*, **325**, 405–11.

Gilbert, F. and Dziewonski, A.M. (1975). An application of normal mode theory to the retrieval of structural parameters and source mechanisms from seismic spectra. *Phil. Trans. Roy. Soc. Lond.*, Ser. A, **278**, 187–269.

Hansen, R.A. (1982a). Simultaneous estimation of terrestrial eigenvibrations. *Geophys. J. Roy. Astron. Soc.*, **70**, 155–72.

Hansen, R.A. (1982b). Observational study of terrestrial eigenvibrations. *Phys. Earth Planet. Int.*, **28**, 29–69.

Hays, J.D., Imbrie, J.I., and Shackleton, N.J. (1976). Variations in the earth's orbit: pacemaker of the Ice Ages. *Science*, **194**, 1121–32.

Herbert, T.D. and Fischer, A.G. (1986). Milankovitch climatic origin of mid-Cretaceous black shale rhythms in central Italy. *Nature*, **321**, 739–43.

Hori, S., Fukao, Y., Kumazawa, M., Furumoto, M., and Yamamoto, A. (1989). A new method of spectral analysis and its application to the Earth's free oscillations: The 'Sompi' method. *J. Geophys. Res.*, **94**, 7535–53.

Houston, H. (1990). Broadband source spectrum, seismic energy, and stress drop of the 1989 Macquarie Ridge earthquake. *Geophys. Res. Lett.*, **17**, 1021–4.

Imbrie, J., Hays, J.D., Martinson, D.G., McIntyre, A., Mix, A.C., Morley, J.J., Pisias, N.G., Prell, W.L., and Shackleton, N.J. (1984). The orbital theory of Pleistocene climate: support from a revised chronology of the marine $\delta(^{18}O)$ record. In *Milankovitch and Climate*, Part 1, Berger, A., Imbrie, J., Hays, J., Kukla, G., and Saltzman, B. (eds). D. Reidel, Hingham, Mass.

Jordan, T.H. (1978). A procedure for estimating lateral variations from low-frequency seismic data. *Geophys. J. Roy. Astron. Soc.*, **52**, 441–55.

Kutzbach, J.E. and Guetter, P.J. (1986). The influence of changing orbital parameters and surface boundary conditions on climate simulations for the past 18,000 years. *J. Atmos. Sci.*, **33**, 1726–59.

Lawson, C.L. and Hanson, R.J. (1974). *Solving Least Squares Problems*, Prentice-Hall, Englewood Cliffs, N.J.

Lindberg, C.R. (1986). *Multiple Taper Spectral Analysis of Terrestrial Free Oscillations*, Ph.D. Thesis, University of California, San Diego.

Lindberg, C.R. and Park, J. (1987). Multiple-taper spectral analysis of terrestrial free oscillations, Part II. *Geophys. J. Roy. Astron. Soc.*, **91**, 795–836.
Lindberg, C.R. and Thomson, D.J. (1990). Commentary on 'A new method of spectral analysis and its application to the Earth's free oscillations: The "Sompi" method'. *J. Geophys. Res.*, **95**, 19 785–8.
Maasch, K.A. (1988). Statistical detection of the mid-Pleistocene transition. *Climate Dynamics*, **2**, 133–43.
Maasch, K.A. and Saltzman, B. (1990). A low-order dynamical model of global climate variability over the full Pleistocene. *J. Geophys. Res.*, **95**, 1955–63.
Masters, G. and Gilbert, F. (1983). Attenuation in the earth at low frequencies. *Phil. Trans. Roy. Soc. Lond.*, Ser. A, **308**, 479–522.
Masters, G., Park, J., and Gilbert, F. (1983). Observations of coupled spheroidal and toroidal modes, *J. Geophys. Res.*, **88**, 10 285–98.
Menke, W. (1984). *Geophysical Data Analysis: Discrete Inverse Theory*, Academic Press, Orlando.
Olsen, P.E. (1986). A 40-million-year lake record of early Mesozoic orbital climate forcing. *Science*, **234**, 842–484.
Park, J. (1986). Synthetic seismograms from coupled free oscillations: the effects of lateral structure and rotation. *J. Geophys. Res.*, **91**, 6441–64.
Park, J. (1987). Asymptotic coupled-mode expressions for multiplet amplitude anomalies and frequency shifts on an aspherical earth. *Geophys. J. Roy. Astron. Soc.*, **90**, 129–69.
Park, J. (1988). Free oscillation coupling theory. In *Mathematical Geophysics*, Vlaar, N.J., Nolet, G., Wortel, M.J.R., and Cloetingh, S.A.P.L. (eds). D. Reidel, Dordrecht.
Park, J. (1990). Observed envelopes of coupled seismic free oscillations. *Geophys. Res. Lett.*, **17**, 1489–92.
Park, J. and Gilbert, F. (1986). Coupled free oscillations of an aspherical, dissipative, rotating earth: Galerkin theory. *J. Geophys. Res.*, **91**, 7241–60.
Park, J. and Herbert, T.D. (1987). Hunting for paleoclimatic periodicities in a geologic time series with an uncertain time scale. *J. Geophys. Res.*, **92**, 14 027–40.
Park, J., Lindberg, C.R., and Thomson, D.J. (1987a). Multiple-taper spectral analysis of terrestrial free oscillations, Part 1. *Geophys. J. Roy. Astron. Soc.*, **91**, 755–894.
Park, J., Lindberg, C.R., and Vernon, F.L., III (1987b). Multiple-taper spectral analysis of high frequency seismograms. *J. Geophys. Res.*, **92**, 12 675–84.
Parker, R.L. (1977). Understanding inverse theory. *Ann. Rev. Earth Plan. Sci.*, **5**, 35–64.
Parker, R.L. (1990). *Inverse Theory*. Unpublished book manuscript.
Parker, R.L., Shure, L., and Hildebrand, J.A. (1987). The application of inverse theory to seamount magnetism. *Rev. Geophys.*, **25**, 17–40.
Prell, W.L. and Kutzbach, J.E. (1987). Variability of the monsoon over the past 150,000 years: Comparison of observed and simulated paleoclimatic time series. *J. Geophys. Res.*, **92**, 8411–25.
Raymo, M.E., Ruddiman, W.F., Backman, J., Clement, B.M., and Martinson, D.G. (1989). Late Pliocene variation in northern hemisphere ice sheets and North Atlantic Deep Water circulation. *Paleoceanography*, **4**, 413–46.
Reinsch, C.H. (1967). Smoothing by spline functions. *Numerische Mathematik*, **10**, 177–83.
Ritzwoller, M., Masters, G., and Gilbert, F. (1986). Observations of anomalous splitting and their interpretation in terms of aspherical structure. *J. Geophys. Res.*, **91**, 10 203–28.
Ruddiman, W.F., Raymo, M.E., Martinson, D.G., Clement, B.M., and Backman, J. (1989). Pleistocene evolution: Northern hemisphere ice sheets and the North Atlantic Ocean. *Paleoceanography*, **4**, 353–412.

Saltzman, B. and Sutera, A. (1984). A model of the internal feedback system involved in late Quaternary climatic variations. *J. Atmos. Sci.*, **41**, 736–45.
Shure, L., Parker, R.L., and Backus, G.E. (1982). Harmonic splines for geomagnetic modelling. *Phys. Earth Plan. Inter.*, **28**, 215–29.
Slepian, D. (1978). Prolate spheroidal wave functions, Fourier analysis and uncertainty – V: The discrete case. *Bell Syst. Tech. J.*, **57**, 1371–1429.
Slepian, D. (1983). Some comments on Fourier analysis, uncertainty, and modeling. *SIAM Rev.*, **25**, 379–93.
Smith, M.F. and Masters, G. (1989). Aspherical structure constraints from free oscillation frequency and attenuation measurements. *J. Geophys. Res.*, **94**, 1953–76.
Stark, P.B., Parker, R.L., Masters, G., and Orcutt, J.A. (1986). Strict bounds on seismic velocity in the spherical earth. *J. Geophys. Res.*, **91**, 13 892–902.
Tarantola, A. (1987). *Inverse Problem Theory*, Elsevier, Amsterdam.
Thomson, D.J. (1982). Spectrum estimation and harmonic analysis. *Proc. IEEE*, **70**, 1055–96.
Thomson, D.J. (1990). Time series analysis of Holocene climatic data. *Phil. Trans. Roy. Soc. Lond.*, **330**, 601–16.
Tichelaar, B.W. and Ruff, L.J. (1990). Rupture process and stress drop of the great 1989 Macquarie Ridge earthquake. *Geophys. Res. Lett.*, **17**, 1001–4.
Walden, A.T. (1990). Improved low-frequency decay estimation using the multitaper spectral analysis method. *Geophys. Prospecting*, **38**, 61–86.
Woodhouse, J.H. (1983). The joint inversion of seismic waveforms for lateral variations in Earth structure and earthquake source parameters. In *Proceedings of the Enrico Fermi International School of Physics, 85*, Kanamori, H. and Boschi, E. (eds), North Holland, Amsterdam.